Fracture processes and in-situ fracture observations in Gipskeuper

Bruchprozesse und in-situ Beobachtungen von Rissen im Gipskeuper

Processus de fracturation et observation des fractures in-situ dans le Gipskeuper

ETH Zürich, Chair of Engineering Geology
Dr. Florian Amann
Dr. Ömer Ündül
Prof. Dr. Simon Löw

Center of Excellence in Mining Innovation, CEMI, Sudbury, Canada
Prof. Dr. Peter Kaiser

August 2013   **1422**

Fracture processes and in-situ fracture observations in Gipskeuper

Bruchprozesse und in-situ Beobachtungen von Rissen im Gipskeuper

Processus de fracturation et observation des fractures in-situ dans le Gipskeuper

ETH Zürich, Chair of Engineering Geology
Dr. Florian Amann
Dr. Ömer Ündül
Prof. Dr. Simon Löw

Center of Excellence in Mining Innovation, CEMI, Sudbury, Canada
Prof. Dr. Peter Kaiser

Impressum

Forschungsstelle und Projektteam

Projektleitung
Dr. Florian Amann, ETH Zürich

Mitglieder
Dr. Ömer Ündül, ETH Zürich
Prof. Dr. Simon Löw, ETH Zürich
Prof. Dr. Peter Kaiser, CEMI

Begleitkommission

Präsident
Matthias Folly, Swiss Federal Roads Office, Ittigen

Mitglieder
Christian Amstad, Consulting Engineer, Zollikerberg
Christian Gammeter, Swiss Federal Roads Office, Ittigen
Dr. Ruth Haas-Nüesch, Karlsruhe Institute of Technology, Karlsruhe
Dr. Matthias Schwotzer, Karlsruhe Institute of Technology, Karlsruhe
Dr. Walter Steiner, B & S AG, Bern

KO-Finanzierung des Forschungsauftrags

Engineering Faculty, Geological Engineering Department,
Istanbul University under the aegis of The Council of Higher Education of Turkey

Antragsteller

Bundesamt für Strassen (ASTRA)

Bezugsquelle

Das Dokument kann kostenlos von http://www.mobilityplatform.ch heruntergeladen werden.

Table of Content

Executive Summary

Several tunnels constructed in sulfate-rich clay rocks revealed severe and costly problems associated with floor heave as a consequence of gypsum precipitation. Previous studies have shown that gypsum precipitation often takes place within pre-existing natural structures or fissures which were created by hoop-stresses and opened as a consequence of radial stress relief. Brittle fracture processes cause a damage zone around an underground excavation in sulfate-rich clay rock when the stress exceeds the crack initiation threshold. Microcracks in the damage zone are seen as a preconditioning factor for gypsum precipitation when sulfate-rich fluids penetrate these fissures and become supersaturated. However, brittle failure processes in sulfate-rich clay rocks and the stress magnitudes required to initiate microcracks were previously not studied in detail, and the hypothesis of brittle fracturing as a major cause for swelling has not been conclusively proven. It was also not studied in detail newly formed fractures actually exist in the vicinity of tunnels in this rock type, and if these fracture may be related to stress fracturing or unloading or propagation of pre-existing discontinuities. Furthermore, the influence of newly formed fractures on fluid flow and gypsum precipitation was not demonstrated.

In this study we test these hypotheses with data from new boreholes and cores drilled into the Gipskeuper formation intersected by the Belchen tunnel in the Swiss Jura Mountains. The investigation primarily focuses on the stress magnitude at which microcracks initiate in Anhydrite-Clay rocks, on factors such as heterogeneities that affect the fracturing processes and strength, and on micro-structural observations below the invert of the Belchen drainage tunnel. This investigation provides insights into the fracture formation mechanisms and its influence on preferential pathways for fluid flow and gypsum precipitation.

Unconfined and confined compression tests with acoustic emission monitoring, and microstructural and mineralogical analyses were used to explain the failure behavior of sulfate-rich clay rock from the Gipskeuper-formation in Switzerland at the laboratory scale. The samples for these analyses were extracted from six boreholes drilled at the Belchen Drainage Tunnel in Switzerland in October 2011. Core and optical televiewer logging, thin section and XRD analyses were used to characterize the rock mass at the tunnel scale in terms of mineralogical composition, discontinuity orientation, discontinuity infillings, and fracture network. The following results have been achieved.

The rock mechanical analyses showed that the failure behavior is dominated by the strength of the clayey matrix where microcracks are initiated. For specimen which showed a heterogeneous rock fabric (e.g. consisting of discrete clay layers and veins with sulfatic fillings), it was observed that the differential stress required to initiate microcracks is dependent on the clay content. For a clay content >7-10% first microcrack are typically initiated at a differential stress ranging between 4 to 13 MPa. Variations in the crack initiation stress are most probably associated with the microstructure and

Anhydrite content of the clayey matrix, and stress or strain heterogeneities developing upon compressive loading. For clay content <7-10%, both, the crack initiation stress and the peak strength increase substantially with decreasing clay content.

The results of triaxial compressive strength tests suggest that for clay content >7% the differential stress at crack initiation is almost independent on the confining stress, and ranges between 4 to 8 MPa. For the same tests the peak strength varied markedly depending on the clay content.

Thin section analyses of specimens after mechanical loading showed, that with increasing differential stress beyond the crack initiation stress, the rock fabric has a considerable influence on fracture growth, fracture coalescence and peak strength. Depending on the vein density, distribution and orientation, growing microcracks eventually get arrested at Anhydrite veins, and cracks aligned with the interface between clayey layers and veins form, or penetrate veins. These cracks often link micro-fractured regions in the specimen. Because Anhydrite veins are much stronger than the clayey matrix, the strength typically increases with increasing vein density, even though microcracks may form at low differential stresses.

The core and optical televiewer analyses showed, that macro- and microscopic open fractures are rarely observed. In a depth range between the tunnel invert and a maximum depth of 2.35m fractures were encountered which were healed with fibrous gypsum. These fractures were solely found in the clayey matrix, and the majority of these fractures could not be related to bedding planes or pre-existing discontinuities. Only few fibrous gypsum veins along natural fractures or bedding planes were found. At depth below 2.35m beneath the tunnel invert all discontinuities were filled with anhydrite. These findings suggest that the majority of the observed fractures in the first 0.7 to 2.35m of the six boreholes are newly formed fractures.

The majority of the newly formed microcracks in the first few decimeters of the boreholes showed alteration rims affecting approximately 0.05-0.1mm of the clayey matrix. Such alteration of the clayey matrix is typically related to fluid flow. Fibrous gypsum was almost exclusively found in these fractures. These findings suggest that these microcracks are interconnected and serve as preferential pathway for groundwater circulation and gypsum precipitation.

Zusammenfassung

Bei zahlreichen Tunnelbauwerken in sulfat-haltigen Tonsteinen führten Sohlhebungen aufgrund von Gipskristallwachstum zu erheblichen und kostenintensiven Problemen. Gipskristallwachstum ereignet sich häufig entlang prä-existenter tektonischer Diskontinuitäten oder Rissen, welche durch Spannungsumlagerungen entstanden sind und sich durch die Entlastung der Radialspannung öffneten. Es wird angenommen, dass spröde Bruchprozesse in sulfat-haltigen Tonsteinen zu einer Auflockerungszone um den Hohlraum führen, wenn die umgelagerten Spannungen die Grenzspannung für Mikrorissbildung überschreiten. Diese Mikrorisse werden als Prä-konditionierungsfaktor für die Kristallisation von Gips gesehen, wenn sulfat-haltiges Wasser in diesen Rissen zirkuliert und eine übersättigte Lösung entsteht.

Sowohl diese Hypothese als auch die für die Mikrorissbildung notwendigen Spannungsmagnituden in sulfat-haltigen Tongesteinen wurden bisher nicht im Detail untersucht. Ebenso wurde bislang nicht nachgewiesen, ob neu entstandene Risse im Nahbereich von Tunnelbauwerken in diesem Felstyp tatsächlich existieren und ob diese Risse allenfalls auf Entlastung oder Fortpflanzung existierender Diskontinuitäten zurückzuführen sind. Zudem konnte bisher nicht gezeigt werden inwiefern neu entstandene Risse einen Einfluss auf die Wasserzirkulation und die Gipsausfällung haben.

Diese Studie befasst sich insbesondere mit den Spannungsmagnituden bei deren Überschreitung die Mikrorissbildung initialisiert wird, den Faktoren (wie Heterogenitäten), welche den Bruchprozess und die Festigkeit beeinflussen, sowie Beobachtungen im Nahbereich eines Tunnels welche auf Rissbildungen und deren Einfluss auf die Wasserwegigkeit und Gipsausfällung hinweisen.

Einaxiale und triaxiale Druckversuche mit Messungen von akustischen Emissionen sowie mikrostrukturelle und mineralogische Analysen wurden herangezogen, um das Bruchverhalten von sulfat-haltigen Tonsteinen der Gipskeuper-Formation im Belchen-Drainagetunnel auf der Laborskala zu klären. Die Proben für die felsmechanischen, mineralogischen und mikrostrukturellen Analysen stammten aus sechs Bohrungen, welche im Oktober 2011 aus der Sohle des Belchen-Drainagetunnels abgeteuft wurden. Basierend auf Kernaufnahmen, Aufnahmen eines optischen Bohrlochscanners sowie Dünnschliff- und XRD- Analysen wurde das Gebirge auf der Tunnelskala hinsichtlich der mineralogischen Zusammensetzung, der Trennflächenorientierungen, etwaiger Trennflächenfüllungen und deren Vernetzung charakterisiert.

Die felsmechanische Laborversuche haben gezeigt, dass das Bruchverhalten von der Festigkeit der tonigen Matrix bestimmt wird, in der erste Mikrorisse entstehen. An Prüfkörper mit einem heterogenen Gefüge aus diskreten Tonsteinlagen und Anhydrit-Venen wurde beobachtet, dass die Differentialspannung zur Initialisierung von Mikrorissen vom Tongehalt abhängt. Bei einem Tongehalt >7-10% entstehen erste Mikrorisse bei einer

relativ konstanten Differentialspannung im Bereich zwischen 4 und 13 MPa. Variationen in der Grenzspannung zur Rissinitialisierung stehen sehr wahrscheinlich im Zusammenhang mit der Mikrostruktur und dem Anhydrit-Gehalt der tonigen Matrix sowie Spannungs- und Dehnungs-Heterogenitäten als Folge zunehmender kompressiver Spannungen. Für geringe Tongehalt <7-10% nehmen sowohl die Grenzspannungen zur Rissinitialisierung als auch die Spitzenfestigkeiten deutlich zu.

Dünnschliffanalysen von Prüfkörpern nach mechanischer Belastung deuten darauf hin, dass bei kompressiven Belastungen oberhalb der Grenzspannung zur Rissbildung die Felsstruktur einen markanten Einfluss auf das Risswachstum, die Risszusammenschliessung und die Spitzenfestigkeiten hat. In Abhängigkeit der Venendichte, der Venenverteilung und Venenorientierung kann das Risswachstum an Anhydrit-Venen stoppen, Risse können anschliessend entlang von Venen entstehen, oder die Venen durchschlagen. Diese Risse führen häufig zur Vernetzung von mikro-geschädigten Regionen im Prüfkörper. Da Anhydrit-Venen grössere Festigkeiten als die tonige Matrix aufweisen, nimmt mit zunehmender Venendichte die Spitzenfestigkeit zu, obgleich erste Mikrorisse bereits bei niedrigen Differentialspannungen entstehen.

Die Analyse der Bohrkerne und die optischen Bohrlochscanner-Aufnahmen im Sohlbereich des Drainagestollens haben gezeigt, dass nur sehr wenige offene, makroskopische oder mikroskopische Risse zu finden sind. Im Bereich zwischen der Tunnelsohle und maximal 2.35m Tiefe wurden Risse angetroffen, welche mit Fasergips verheilt waren. Derartige Risse sind ausschliesslich in der tonigen Matrix zu finden und konnten keinem prä-existierenden Risssystem oder schichtungsparallelen Diskontinuitäten zugeordnet werden. Nur wenige natürliche Strukturen (Störzonen) waren mit Fasergips verfüllt. Diese Erkenntnisse zeigen, dass die in den ersten 0.7 bis 2.35m der sechs Bohrungen angetroffenen Risse neu entstanden sind.

Der Grossteil der neu entstandenen Mikrorisse in den oberen Bohrlochdezimetern zeigten zudem Reaktionsränder von etwa 0.05-0.1mm Mächtigkeit. Fasergips wurde nahezu ausschliesslich in solchen Rissen gefunden. Die chemische Umwandlung der tonigen Matrix wird im Zusammenhang mit Wasserzirkulation gesehen. Diese Erkenntnisse lassen den Schluss zu, dass die beobachteten Mikrorisse vernetzt sind und präferentielle Fliesswege für die Wasserzirkulation und die Gipsausfällung darstellen.

Résumé

De nombreux tunnels construits dans des argilites riches en sulfates rencontrent des problèmes coûteux associés au soulèvement du radier en conséquence du gonflement des roches lié à la précipitation de gypse. La précipitation du gypse a souvent lieu dans des diaclases tectoniques préexistantes ou dans des fissures nouvellement formées par la concentration des contraintes tangentielles et le relâchement des contraintes radiales. Il est supposé que les processus de rupture fragile causent une zone endommagée autour d'une excavation sous-terraine dans des argilites riches en sulfate lorsque le niveau des contraintes dépasse le seuil d'initiation de fracture. La présence de micro-fractures dans la zone endommagée est un facteur de pré-conditionnement pour la précipitation de gypse facilitant la percolation dans ces fissures d'eaux sous-terraines saturées en sulfates. Cependant, les processus de rupture fragile dans les argilites riches en sulfate sont peu étudiés et l'hypothèse de rupture fragile ainsi que le niveau des contraintes nécessaire à initier des micro-fractures restent à vérifier. Il n'existe pas d'étude détaillée qui montre la présence de fractures nouvellement formées au voisinage de tunnels excavés dans ce type de roche et qui indique si ces fractures sont causées par la concentration des contraintes, le relâchement des contraintes ou la propagation de discontinuités préexistantes. De plus, l'influence de fractures nouvellement formées sur les écoulements de fluides et la précipitation du gypse n'est pas démontrée.

Cette étude se concentre principalement sur la détermination du seuil d'initiation de fracture, l'évaluation de facteurs tels que les hétérogénéités influençant les processus de fracturation et la résistance à la rupture, ainsi que l'observation des indicateurs liés à la formation de fractures dans le voisinage du tunnel et leurs influence sur les chemins d'écoulement et la précipitation du gypse.

Des tests en compression avec et sans confinement accompagnés de l'enregistrement des émissions acoustiques et d'analyses minéralogiques et microstructurales ont été effectués pour appréhender le comportement en rupture à l'échelle du laboratoire des argilites riches en sulfates du Gipskeuper suisse. Les échantillons pour ces analyses ont été extraits de 6 forages carottés au tunnel de drainage de Belchen en Suisse en octobre 2011. Des relevés de carotte, des mesures au televiewer, ainsi que des analyses en lame mince et aux rayons X permirent de caractériser le massif rocheux à l'échelle du tunnel en terme de composition minéralogique, d'orientation des discontinuités, du remplissage des discontinuités et du réseau de fractures.

Les tests mécaniques en laboratoire indiquent qu'à bas niveau des contraintes différentielles le comportement à la rupture est dominé par la résistance de la matrice argileuse où les micro-fractures sont initiées. Pour les échantillons contenant une fabrique hétérogène (p. ex. l'alternance de feuillets argileux distincts et de veines d'anhydrite ou de dolomite), le niveau des contraintes requis pour initier des micro-fractures dépend du contenu en

argile. Pour des pourcentages d'argile >7–10%, les premières micro-fractures sont initiées à un niveau des contraintes différentielles relativement constant de 4 à 13 MPa. Les variations du seuil d'initiation de fracture sont très probablement due à la présence de microstructures et aux variation du contenu en anhydrite de la matrice argileuse. Celles-ci induisent le développement d'hétérogénéité des déformations et de contraintes lors d'un chargement en compression. Pour des pourcentages d'argile <7–10%, le seuil d'initiation de fracture et la résistance maximale à la compression augmentent sensiblement avec un déclin du contenu en argile.

Les résultats des tests triaxiaux en compression indiquent que pour des contenus en argiles >7%, le niveau des contraintes différentielles au seuil d'initiation de fracture est indépendant de la pression de confinement et est d'environ 4 à 8 MPa. Pour les mêmes tests, la résistance maximale à la compression varie considérablement en fonction de la teneur en argiles.

L'analyse en lame mince d'échantillons ayant été testés en compression indiquent qu'avec l'augmentation des contraintes différentielles au-delà du seuil d'initiation de fracture, la fabrique a une influence considérable sur la propagation des fractures, leur coalescence et la résistance maximale de l'échantillon. Selon la densité, la distribution et l'orientation des veines, la propagation de micro-fractures est arrêtée par les veines d'anhydrite et les fractures se forment à l'interface des couches argileuses et des veines ou alors pénètre les veines. Ces fractures connectent des régions micro-fracturées distinctes de l'échantillon. Du fait que les veines sont bien plus résistantes que la matrice argileuse, la résistance augmente avec l'augmentation de la densité de veines, même si les micro-fractures se forment à de faibles niveaux des contraintes différentielles.

Les analyses du relevé des carottes et des images de televiewer indiquent que des fractures ouvertes, macro- ou microscopiques, sont rarement observées. Pour les profondeurs jusqu'à 2.35m sous le radier, des fractures remplies de gypse fibreux ont été observées. Ces fractures se situent exclusivement dans la matrice argileuse et ne sont généralement pas associées avec des discontinuités préexistantes. Seule une quantité limitée de gypse fibreux a été observée le long de diaclase tectonique, ou de plans de faille ou de stratification. A des profondeurs excédant 2.35m sous le radier, toutes les discontinuités sont remplies d'anhydrite. Ces observations suggèrent que la majorité des fractures observées dans les premières dizaines de centimètre des forages sont des fractures nouvellement formées.

Ces fractures présentent des halos d'altération de la matrice argileuse d'une largeur d'environ 0.05 à 0.1mm. Le gypse fibreux a été observé pour ainsi dire exclusivement dans ces fractures. L'altération de la matrice argileuse est liée probablement aux circulations de fluides. Ces observations indiquent que les micro-fractures sont interconnectées et forment des chemins d'écoulement préférentiels pour la circulation des eaux sous-terraines et la précipitation du gypse.

1 Final Report

1.1 Introduction

Several tunnels excavated through sulfate-rich clay rocks revealed severe and costly problems during construction and operation. These problems are mostly associated with gypsum precipitation from a supersaturated sulfate solution [1], [2], [3], causing volume expansion and invert heaves of up to several decimeters within weeks, months or years after tunnel excavation [4], [5], [6]. Observations in these tunnels also showed that the swelling phenomenon is limited to the tunnel invert [6], [7].

Alonso and Berdugo [2] analyzed geomechanical and mineralogical data of various tunnels in sulfate-rich clay rocks focusing on processes causing supersaturated groundwater conditions, and rock degradation in a finite zone beneath the tunnel invert. They defined degradation as natural and anthropic factors causing the opening of fissures, volume change, and reduction of strength and stiffness. Alonso and Berdugo [2] found evidences that precipitation of gypsum is associated with preferential flow of sulfate-rich groundwater in fissures and unloaded slickenside surfaces, and processes causing supersaturated pore water (e.g. due to evaporation). Newly formed discontinuities are considered to have opened as a consequence of mechanical stress relief. Alonso and Berdugo [2] concluded that damage induced by stress redistribution around a tunnel in sulfate-rich clay rocks enhance the potential for gypsum precipitation.

These findings are consistent with observation made by Grob [8] during the construction of the Belchen Highway tunnel, and mineralogical and structural investigations of Madsen and Nüesch [9] and Madsen et al [10]. From micro-structural observation [10] concluded, that the short water transport time along brittle deformed clay layers causes a high rate of transformation of anhydrite to gypsum. They also observed that the transformation-rate of anhydrite into gypsum was accelerated in anhydrite-bearing brittle deformed cataclastic clay rocks. Thin section analyses of specimens utilized for long-term swelling test by [9] showed that precipitation of gypsum often occurs in clay layers that were originally sulfate-free. Their studies also showed that gypsum precipitation occurs predominately in existing fissures and along clay layers. Similar observations at the tunnel scale have been reported by Grob [8]. During the construction of the Belchen Highway Tunnel several shafts of 2-2.5 m depth were excavated at the tunnel invert. The geological assessment revealed that water circulation and crystal growth took place in "hair-line cracks within deformed clay layers". Crystal growth in these cracks often causes further crack-extension and related crack-expansion and thus creates further crystal growth potential [8].

The aforementioned studies consistently suggest that discontinuities such as cracks or fissures in the clayey matrix, or unloaded tectonic structures are preconditioning factors for preferential flow of sulfate-rich water, and gypsum precipitates when the groundwater eventually becomes supersaturated. These discontinuities can either be related to unloading and opening

of pre-existing tectonic structures such as slickenside surfaces or joints [2], [11], or stress-induced fracturing.

Excavation-induced stress fracturing was suggested by Kaiser and Kim [12] to play a key role in preconditioning, and thus increasing the swelling potential of sulfate-rich clay rock types. They hypothesized that sulfate-rich clay rocks may fail in a brittle manner by developing extensional fractures in deviatorically stressed zones near tunnels, particularly in zones where the confinement is low. These extensional fractures are considered to increase the hydraulic conductivity, and serve as a preconditioning factor for gypsum precipitation when supersaturated groundwater approaches the fractured zone beneath the tunnel invert. The hypothesis is based on research on fracture processes in hard crystalline and sedimentary rock types under compressive load on both, the laboratory and the tunnel scale. Compression tests on cylindrical specimen showed that brittle rocks fail as a consequence of microcrack initiation, propagation and eventually coalescence when a critical microcrack density is approached (Figure 1.1). Under unconfined compressive loads, extensional microcracks are initiated at an axial stress of approximately 0.3 to 0.6 of the unconfined compressive strength (UCS) (Figure 1.1); after [13], [14], [15] [16], [17], [18], [19], [20], [21], [22].
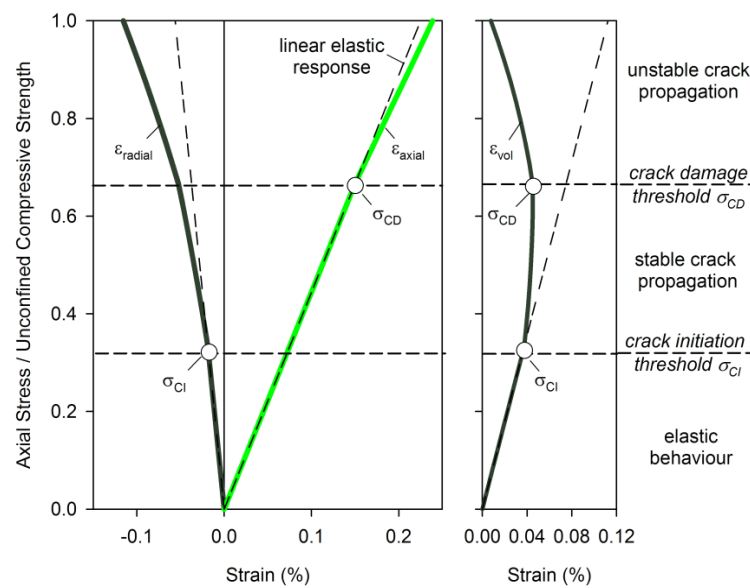
Figure 1.1 Stress and behavior thresholds of a brittle failing rock under unconfined compression according to Brace et al. [14].

These microcracks are initially predominantly aligned with the maximum principal stress orientation. Crack initiation at σ_{CI} is accompanied by dilatancy, and thus the volumetric strain curve deviates from linearity (Figure 1.2). At this stage of brittle failure, the microcracks grow in a stable manner [19]. With increasing stress or strain, accumulation of microcracks eventually leads to a volumetric strain reversal (Figure 1.1) which is typically observed at between 0.7 and 0.9 –times the peak strength [22]. The volumetric reversal point is also called the crack damage threshold and defines the onset of unstable crack growth [19]. With further increase in axial load mi-

crocracks accumulate, reach a critical crack density, and the specimen ultimately fails by splitting or kinkband-type shear failure at higher confinement.
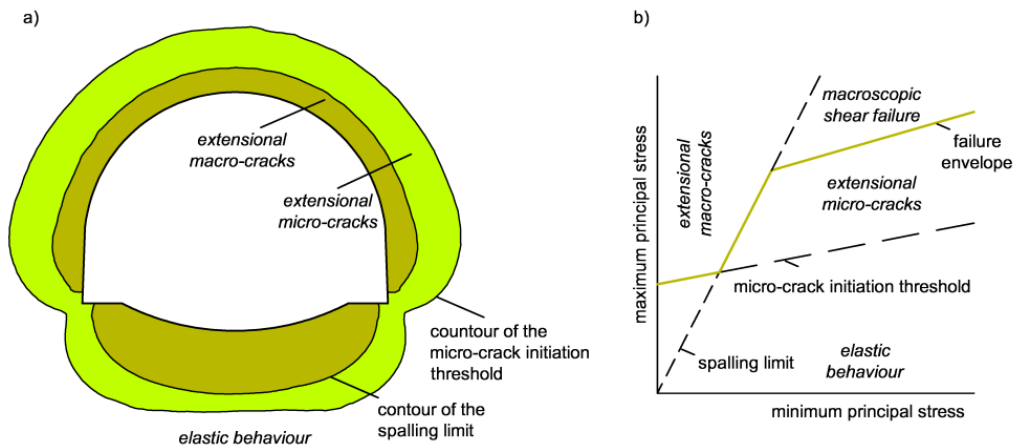
Figure 1.2 a) Illustration of zones of rock mass failure around tunnel in massive to moderately jointed brittle rocks (A hydrostatic stress field is assumed for the illustration); b) assumed rock mechanical processes underpinning the failure behavior around tunnels in massive or moderately brittle rocks at depth[22], [23], [24].

These micro-mechanical observations explain rock mass behavior such as spalling or strainbursting of tunnel walls in massive to moderately jointed, highly stressed brittle rocks [22], [23], [24]. Below the microcrack initiation threshold the rock mass is undisturbed and behaves elastically (Figure 1.2b). The microcrack initiation threshold is relatively insensitive to confinement and thus, the differential stress required to initiate microcracks is almost constant with increasing confining stress [22], [24]. When this threshold is exceeded, and the confining stress is low (to the left of the spalling limit as defined by [25], Figure 1.2b), extensional fractures sub-parallel to the tangential stress orientation are initiated. The stress required to form macro-fracture in the low-confinement zone around a tunnel in brittle rock is substantially below the intact laboratory strength [22], [24] [25]. At higher confinement (to the right of the spalling limit, Figure 1.2b) accumulation of microcracks eventually leads to microcrack coalescence when a critical crack density is reached and eventually macroscopic shear failure.

Extensional fracturing around tunnels was observed in several rock types such as granite, gneiss, limestone, sandstones (i.e. [12], [23], [26], and clay shale, for example in Opalinus Clay or Tournemire shale [27], [28], [29], [30], [31], [32], [33], [34], [35]. Due to observations of extensional fracturing in these clay rocks, the above outlined principals of brittle fracturing were applied to numerical models to conceptually analyze the hypothesized failure mechanism for tunnels in sulfate-rich clay rock ([23], [36], [37], [38], [39]). [38] and [39] showed that the extension of the zones where extensional fracturing is likely to occur (for the assumed σ_{CI} and in-situ stress) have dimensions similar to zones beneath the tunnel inverts where swelling strains were measured. They concluded that brittle extensional fracturing may cause a damage zone with an increased hydraulic conductivity beneath the tunnel invert allowing water circulation and gypsum precipitation when

sulfate-rich water reaches the damaged zone.

However, the failure processes in sulfate-rich clay rocks were not studied experimentally so far, and the hypothesis of brittle fracturing as well as the stress magnitudes required to initiate microcracks as assumed in above studies are not yet proven. It was also not studied in detail if newly formed fractures actually exist in vicinity of tunnels in this rock type, and if these fracture may be related to stress fracturing or unloading or propagating of pre-existing discontinuities. Furthermore, the influence of newly formed fractures on fluid flow and gypsum precipitation was not demonstrated.

1.2   Key questions and report structure

This study was initiated to investigate fractures and fracture processes in sulfate-rich clay rock. The study is primarily focused on the stress magnitude at which microcracks initiate, factors such as heterogeneities that affect the fracture processes and peak strength, and observations in vicinity of a tunnel which might give evidence on fracture formation and its relation to fluid flow and gypsum precipitation. The following key questions are addressed in this report:

- At which differential stress will the failure process be initialized?
- What is the influence of heterogeneities on the failure process?
- Can newly formed fractures be observed in vicinity of the Belchen Drainage tunnel?
- Is there any evidence for a relationship between discontinuities/fractures, fluid flow and gypsum precipitation?
- Are these fractures related to extensional fracturing under compression?

This report is subdivided into two parts associated with the scale of investigation. The first part (chapter 3.1) addresses the mechanical behavior of sulfate-rich clay rock under confined and unconfined compression at the laboratory scale. The second part (chapter 3.2) of this report is related to the tunnel scale, and addresses in-situ observations, mineralogical and microstructural analyses.

2 Methods

2.1 Field investigation

2.1.1 Drilling, sampling storage and handling

The samples for this study were extracted from six boreholes (B) drilled at the Belchen Drainage Tunnel in Switzerland in October 2011 (Figure 2.3). The 84 mm diameter cores were drilled with compressed air cooling to obtain high-quality specimens for mechanical laboratory tests. Four boreholes with a final depth of 5 m were approximately 20° inclined in respect to vertical, and two boreholes were vertical and 10 m in length (Figure 2.3). All cores taken from double-tube core barrels were hermetically sealed with vacuum-evacuated foil immediately after core extraction and core description. These sealed cores were stored in core boxes and protected against dynamic perturbation during transport utilizing air pillows and foam.
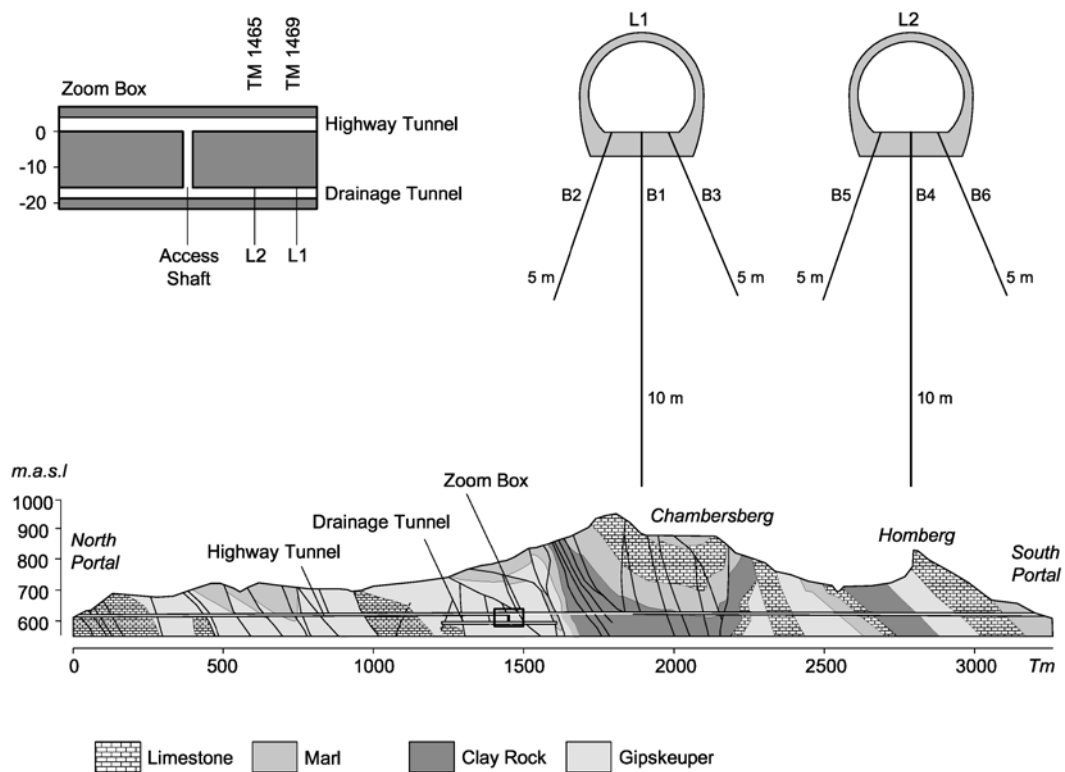
Figure 2.3 Simplified geological cross section along the Belchen Highway Tunnel (according to [4]) showing the location of boreholes (B) drilled from the Belchen Drainage Tunnel to extract samples for this investigation.

2.1.2 Optical Televiewer logging

Continuous, detailed and scaled 360° true-color images of the borehole walls were performed by *TERRATEC-Geophysical* Services in the six boreholes. Prior to logging the borehole walls were thoroughly cleaned with compressed air and a *Slimhole Optical Televiewer OPTV52* was utilized. The Optical Televiewer (OPTV) was operating at its maximum image resolution for the given borehole diameter of 100mm (vertical resolution: 0.5mm/pixel; horizontal resolution: 0.25mm/pixel). During the OPTV logging the image

was instantly oriented to magnetic north by a three axis compass.

Any planar discontinuity intersecting the borehole appears as a trace of sinusoidal shape on the unwrapped image. The amplitudes of the traces determine the dip of the planes. The horizontal position of the maximum and minimum of the traces determines the dip direction of the planes. The analyses of structure orientations (dip-direction and dip) from these images were performed with the Software *WellCad Version 2.0*.

For discontinuities with a short trace length on the unwrapped OPTV image on the cm- scale or an irregular trace the dip and dip direction could not be determined with a sinusoid fit. All discontinuities were mapped at their actual depths and considered for the development of geological models. After core unsealing and sample extraction for mechanical and mineralogical analyses, the results obtained from OPTV logging were verified through a detailed core analyses and description.

2.2 Mineralogical and micro-textural analyses

2.2.1 X-Ray diffraction analyses

123 powder samples for X-ray diffraction (XRD) analysis were prepared by crushing and milling. Samples were crushed to a grain size < 0.4 mm with a jaw breaker and homogenized. A representative aliquot was then milled with an agate mill to a grain size < 20 μm. Mineralogy of the samples was determined on powder samples with X-ray diffraction analysis using a *Bruker AXS D8 Advance Diffractometer* equipped with a *Lynxeye Super Speed Detector*, and a *Philips PW1820 Diffractometer*. The radiation used was Cu–Kα, and samples were scanned from 5° to 90° 2Theta with a step size of 0.02° 2Theta. The counting time was 4s. All XRD analyses were coupled with Rietveld refinement (software *AutoQuan - GE SEIFERT*) using the following phase compositions determined with the software *DIFFRAC-plus* (*BRUKER AXS*): Anhydrite, Gypsum, Celestine, Chlorite, Quartz, Illite, Dolomite, Magnesite, Muscovite, Orthoclase, Plagioclase Albite, Pyrite and Smectite.

2.2.2 Wet chemical analyses

The same powder samples utilized for XRD analyses were also used for wet chemical analyses. The 123 powder samples were dried to constant weight under ambient conditions. In a subsequent step these samples were dried to constant weight in a desiccator. As drying agent P_2O_5 was utilized to extract water adsorbed by clay minerals. Following this process, the samples were placed in an oven of 200°C for 24 hours to extract the mineral water of gypsum. After cooling the samples in a desiccator the final weights were measured. The Gypsum water content was then calculated from the mass difference of the samples after P_2O_5 drying and oven drying. After these steps dried powder samples with varying weights of 0.2-0.25g were separated and added into 100ml ultra-purified water to dissolve sulfate. This mixture was kept at a temperature of 22°C until a constant electric conductivities was reached. The total sulfate content was measured utilizing Ion Chromatography.

A comparison between the results obtained from wet chemical analyses with XRD analyses from the same samples revealed substantial discrepancies. The reasons for the discrepancy might be related to clay minerals (for example Calcium-Smectite) which may not loose water during drying in the desiccators. Because of the observed discrepancy this data were not considered in this report.

2.2.3 Thin section preparation

Thin sections were prepared from selected specimens either before or after mechanical testing. Prior to thin section preparation, a low viscous, blue stained epoxy resin was drawn into the samples under a moderate vacuum. This resin penetrates cracks in the samples and allows for a better identification of cracks under the microscope. All thin sections were prepared under dry conditions.

2.3 Rock mechanical laboratory investigation

2.3.1 Specimen preparation and selection

The Gipskeuper formation is characterized by an extensive heterogeneity, folding, and physical anisotropy on multiple scales (e.g. mm- to m-scale). Therefore, cores taken from boreholes in this geological formation show various bedding plane orientations and mineralogical compositions. The mineralogical composition encountered in the cores of the six boreholes spans from almost pure anhydrite/dolomite sections (clay content < 5%) to clay rock sections with clay content up to 80%. Depending on the mineralogical composition and the orientation of the load axis in respect to the bedding plane or vein/layer orientation, rock mechanical properties may vary widely. Therefore 34 mm cores were extracted from the 84 mm diameter cores by over-coring under dry conditions to obtain four specimen geometries (Figure 2.4):

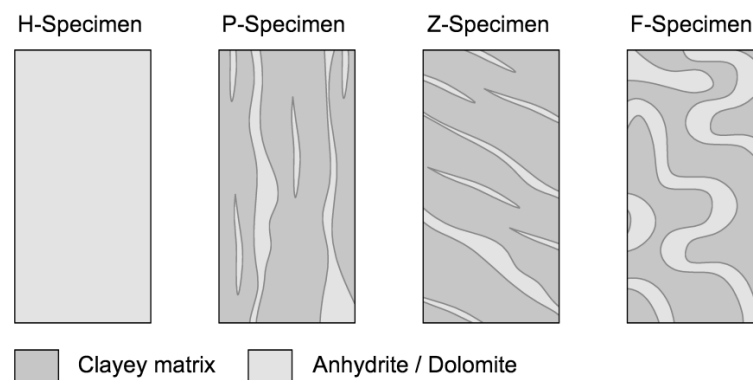*Figure 2.4 Specimen geometries and nomenclature utilized to categorize specimens for unconfined and confined compression tests.*

(1) H-specimens: specimens with a homogeneous rock fabric without distinct clay layers

(2) P-specimens: the load axis is oriented approximately parallel to the bedding orientation or the orientation of veins or layers (e.g., within ± 5° to 10°).

(3)   Z-specimens: the loading axis is oriented approximately 35° to 55° with respect to the bedding plane orientation or the orientation of veins or layers; and

(4)   F-specimens: specimens, where bedding planes, veins or layers are folded. For this specimen type the load axis has various orientations in respect to the rock fabric.

Note, that on the specimen scale heterogeneities can be continuous (layers) or discontinuous (veins). For unconfined compressive strength tests specimens were selected as to investigate mechanical properties and behavior for the range of rock fabric and mineralogical composition encountered in the boreholes. Almost pure anhydrite/dolomite specimens with a macroscopic homogeneous rock fabric and specimens with high content of clay and heterogeneous rock fabric were considered as end-members for the strength and failure behavior. Specimen selection for confined compressive strength tests was based on core logging and limited to heterogeneous rock fabric (e.g., specimens with distinct layers of clay rock and stiff heterogeneities).

Rock mechanical properties may degrade at shallow depth below the tunnel invert due to unloading, swelling or slaking. A series of thin sections taken from different borehole depth was analyzed and revealed that specimens taken below a depth >2.5m contain no microcracks. Samples taken above a borehole depth <2.5m showed microcracks. Thus, only specimens taken from a depth >2.5m below the tunnel invert were used for mechanical tests.

For the unconfined tests two specimen diameters were utilized; 84mm and 34 mm diameter specimens. For confined tests only 34mm diameter specimens were used. All specimens were cut under dry conditions at the Institute of Geotechnical Engineering at the Swiss Federal Institute of Technology in Zurich using a rigid prismatic specimen-holder and an electronically controlled diamond-saw *Type DRAMET BS 270*. The constant band rotating speed (1200 m/min), the constant feed rate (4 mm/min) and the thin metal band (0.7mm) populated with diamonds at both sides of the cutting edge allows for vibrationless cutting and polishing. After cutting the parallelism of the end-faces met the requirements described in [40]. The environmental exposure time of the specimens was minimized through a rigorous preparation procedure, and immediate sealing of the specimens between subsequent preparation steps.

2.3.2   Unconfined compressive strength tests

Unconfined compressive strength tests were performed in the rock mechanical laboratory of the Chair of Engineering Geology at the Swiss Federal Institute of Technology in Zurich. A modified 2000 kN *Walter and Bai* servohydraulic rock testing device with digital feedback control was utilized. Axial and circumferential strain gages were mounted onto the specimen at half of the specimen height to eliminate the influence of end effects on the strain measurements (Figure 2.5). Two axial strain gages (Type *BD 25/50, DD1*) were firmly attached on opposite sides of the specimens. The measurement base-length was 50mm for 84mm diameter specimens, and 35mm for

34mm diameter specimens. The radial strain (ε_{rad}) was calculated from the displacement measured by a single gage (Type *3544-150M-120m-ST*) attached to a chain wrapped tightly around the specimen (Figure 2.5). The circumferential displacement rate was utilized as feedback signal for controlling the load throughout the failure of the specimen. The axial load was increased in such a way as to give a constant circumferential displacement rate of 0.05 mm/min. Before testing of the rock specimens all strain gages and the load cell were calibrated.
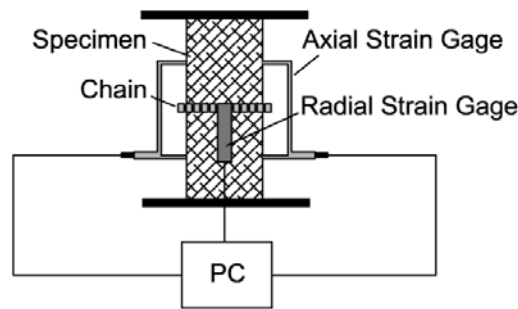
Figure 2.5 Monitoring set-up for unconfined compression stress tests

2.3.3   Confined compressive strength tests

Confined compressive strength tests were performed in the Rock Mechanics Laboratory at the Swiss Federal Institute of Technology in Lausanne. A 2000 kN *Walter and Bai* servo-hydraulic rock testing device with digital feedback control was used. The axial displacement was measured with a 20mm *HBM LVDT* (Figure 2.6) and was used as feedback signal for controlling the load throughout the failure of the specimen. The selected rate was 0.001 mm/s. During the test the volume change in the Hoek cell was continuously measured with an accuracy of $0.1 cm^3$. The oil volume changes were utilized to calculate the volumetric strain ($\varepsilon_{vol,oil}$) of the specimen assuming a cylindrical deformation of the specimen.
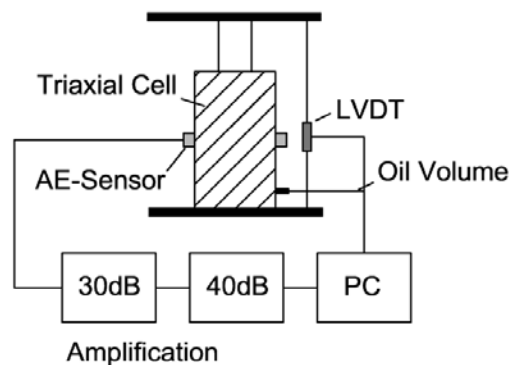
Figure 2.6 Monitoring set-up for triaxial tests. AE: Acoustic Emission Monitoring; LVDT: Linear Variable Differential Transformer; PC: Personal Computer (transient recorder)

For this study four confining stress levels were utilized: 1, 2, 4 and 8 MPa. Prior to deviatoric loading, the axial load and the confining stress were in-

creased simultaneously to establish the predefined hydrostatic stress conditions. Deviatoric loading was applied by increasing the axial load as the confining stress was kept constant.

2.3.4 Determination of the onset of dilation

The onset of dilation in brittle rocks is often associated with micro-cracking and a disproportional increase of the lateral strain in respect to the axial strain. Different methodologies were developed since the 1960's to establish the onset of dilation based on the stress-stain response or micro-acoustic activity [14], [17], [19], [20], [41], [42].

For the unconfined compression tests performed in this study two strain-based methods were utilized, which have been shown to give accurate estimates of the onset of dilatancy [31], [42]. The two different strain-based approaches are illustrated in Figure 2.7a and b.

Method I: [14] suggested that the onset of dilation can be established by examining when the stress - volumetric strain curve deviates from its linear portion at low axial stress (Figure 2.7a). Volumetric strain (ε_{vol}) was calculated from the sum of the arithmetic mean of the two axial strains (ε_{axial}) plus two times the radial strain ($\varepsilon_{axial} + 2\varepsilon_{radial}$).

Method II: [20] applied the same principals as [14] to the radial strain curve. The onset of dilatancy is taken at the point where the stress - radial strain curve deviates from linearity (Figure 2.7b).

In confined compressive strength tests the micro-acoustic activity was examined to establish the onset of micro-cracking as suggested by [41] and illustrated in Figure 2.8a. A *Euro Physical Acoustics AE-system* was utilized. Two 17 mm diameter broad-band piezoelectric sensors (Type *Euro Physical Acoustics WSa*) with a main sensitivity between 10-1000 kHz were firmly affixed on the triaxial cell (Figure 2.6). Amplification was achieved in two stages: The first stage was a pre-amplifier with a 30 dB gain. Before the signal enters the transient recorder, a second stage of amplification was applied with a 40 dB gain. Recording of the data was triggered when the signal amplitude exceeded a pre-defined amplitude threshold. In addition to the micro-acoustic activity, the oil-volume gain and loss from the Hoek cell during deviatoric loading was used to define the onset of dilation according to the method suggested by [14] (Figure 2.8). It was assumed that due to the short test duration temperature variations in the laboratory do not have a significant effect on the volume strain. The data show considerable scatter (Figure 2.8). Thus, only test results with a high signal-to-noise ratio were analyzed.
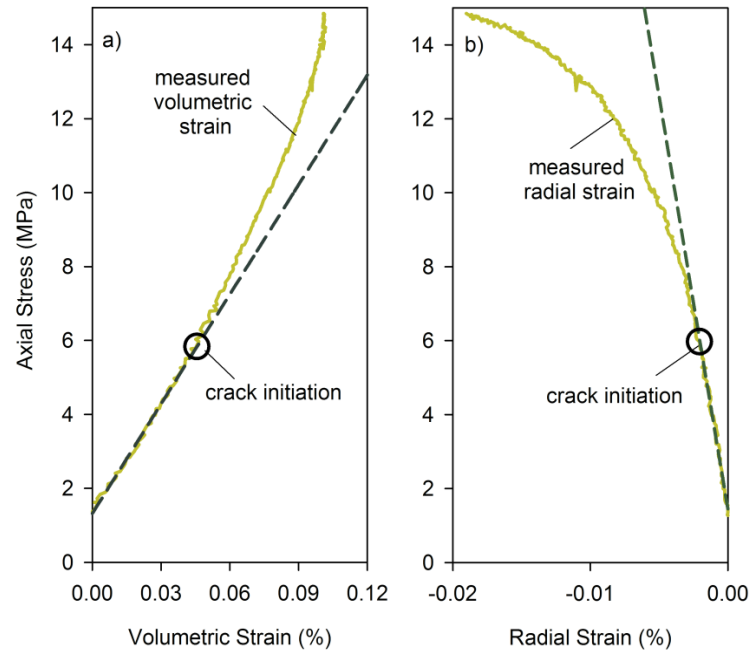
Figure 2.7 Methodology for determining the crack initiation threshold in un-confined compression tests by examining a) the volumetric strain response according to [14]), and b) the radial strain response according to [20]). The dashed lines represent the linear trend.
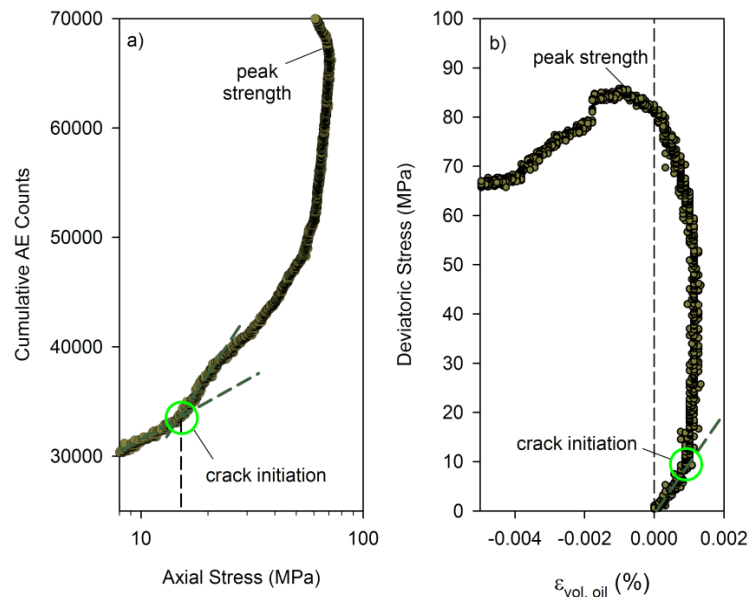
Figure 2.8 Methodology for determining the crack initiation threshold in con-fined compression tests by examining a) acoustic emission data according to [41]), and b) the volumetric strain response obtained from oil volume gain or loss in the Hoek-cell during deviatoric loading. The dashed line in b) rep-resents the linear trend at low deviatoric stress.

3 Results and Interpretation

3.1 Rock mechanical laboratory testing

3.1.1 Specimen characterization

Test specimens are macroscopically characterized by a heterogeneous rock mass fabric (except H-specimen) consisting of a sequence of clay rock (clayey matrix) and varying frequencies of Anhydrite veins or layers (Figure 3.9). Both, the thickness and trace length of Anhydrite veins in the clay matrix ranges on the sub-mm- to cm- scale. In general the mineralogical composition is dominated by the mass fractions of Anhydrite and clay minerals. With increasing clay content the Anhydrite content typically decreases and vice-versa. In other words, specimens with low clay content generally contain a higher density of Anhydrite veins.

Figure 3.9 Typical rock fabric of the test specimens

3.1.2 Rock mechanical properties

The results for unconfined compressive strength values (*UCS*), elastic properties (Young's modulus *E* and Poisson's value υ), the axial stress at the onset of dilation (e.g. crack initiation threshold σ_{CI}), and the mass fraction of clay minerals are summarized in Appendix I.1. The unconfined compressive strength ranges between 5.6 and 151 MPa. Values at the lower strength limit were obtained from specimens that failed through the clay matrix. The upper strength limit was obtained from a specimen containing up to 84% of Anhydrite, and a macroscopically homogeneous rock fabric. The Young's Modulus and Poisson's ratios taken from the axial and radial strain curves at low axial stresses (e.g. axial stresses below σ_{CI}) range from 2.8 to 85.7 GPa and 0.06 to 0.21, respectively.

The UCS limits are considered as end-members and represent the strength of the clayey matrix and Anhydrite veins/layers. Since the clayey matrix is substantially weaker than the veins, it is further assumed that initial fracture processes are related to the mechanical properties of the clay rock.

Confined (triaxial) compressive strength tests were performed on specimens with a heterogeneous fabric (i.e., fabric with distinct layers of clay rock and Anhydrite heterogeneities) using confining stresses ranging between 1 and 8 MPa. The resulting Young's modulus, peak strength, Poisson's value,

the axial stress at the onset of dilation, and the mass fraction of clay minerals obtained from 15 triaxial tests are summarized in Appendix I.2.The Young's Modulus and Poisson's ratios range from 5.0 to 64.9 GPa and 0.07 to 0.37, respectively.

3.1.3 Microcrack initiation

Figure 3.10 shows the relationship between *UCS* and σ_{Cl}. For the range of unconfined compressive strength values between 5.6 and approximately 65 MPa, σ_{Cl} increases with increasing *UCS* at a rate of about 3:10 (trend line is shown in Figure 3.10). In this range of *UCS*, the axial stress at crack initiation varies between 4 and 13 MPa. In the range of *UCS* between 65 and 75 MPa, the crack initiation stress σ_{Cl} increases substantially, and beyond this *UCS*-range (H-specimens) σ_{Cl} seems to again increase at a rate of 3:10 (even though data is limited in this range; dashed trend line is shown in Figure 3.10).
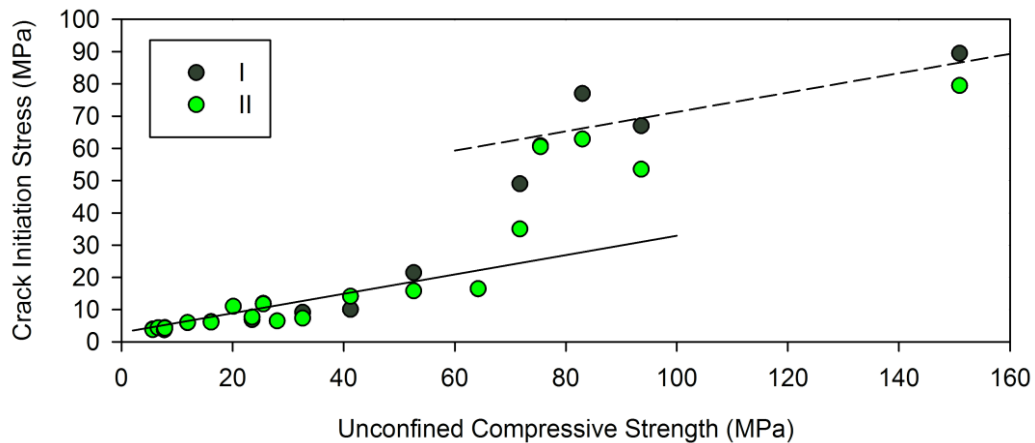
Figure 3.10 Unconfined compressive strength in relation to the axial stress at the onset of dilation (crack initiation stress); I: determined from the volumetric strain response according to [14]; II: determined from the radial strain response according to [20].

The clay content of the specimen was used to show the influence of mineralogical composition on σ_{Cl} (note that with decreasing clay content the Anhydrite vein density increases). Figure 3.11 shows the dependency of σ_{Cl} on the mass fraction of clay minerals. Depending on the mass fraction of clay minerals two distinctly different domains were identified (Figure 3.11): a Domain I, where the clay content is <7-10%, and a Domain II, where the clay content is greater. When the clay content exceeds 7 to 10% (Domain II) σ_{Cl} shows little scatter and is almost constant at 7 MPa (Figure 3.11). The data suggests that the specimen geometry is of minor relevance for the crack initiation stress when the clay content is >20%.

For a clay mineral content <7-10% (Domain I) σ_{Cl} increase substantially with decreasing clay content (Figure 3.11), and thus increasing Anhydrite content. In Domain I, σ_{Cl} decreases in an almost linear manner, even though the scatter is high at the transition between the two Domains.

The clay content for triaxial specimen ranges between 6.7 and 33.8%, and

thus the specimen belong to Domain II and the transition between Domain I and II (Figure 3.11). Figure 3.12 shows the onset of micro-cracking (dilation) at σ_{CI} under triaxial compression in a principal stress (Figure 3.12a) and differential stress diagram (Figure 3.12b). Both, crack initiation obtained from micro-acoustic emission monitoring and the volumetric strain response are shown. It can be seen that with increasing confining stress the axial stress at σ_{CI} tends to slightly increase with a slope of 1.15. The differential stress at σ_{CI} is, however, almost independent of the confinement (Figure 3.12b; slope of 0.15), and ranges between 4 to 8 MPa. This range is consistent with σ_{CI}-values obtained from unconfined compression test on specimens with a clay content exceeding 7 to 10%.
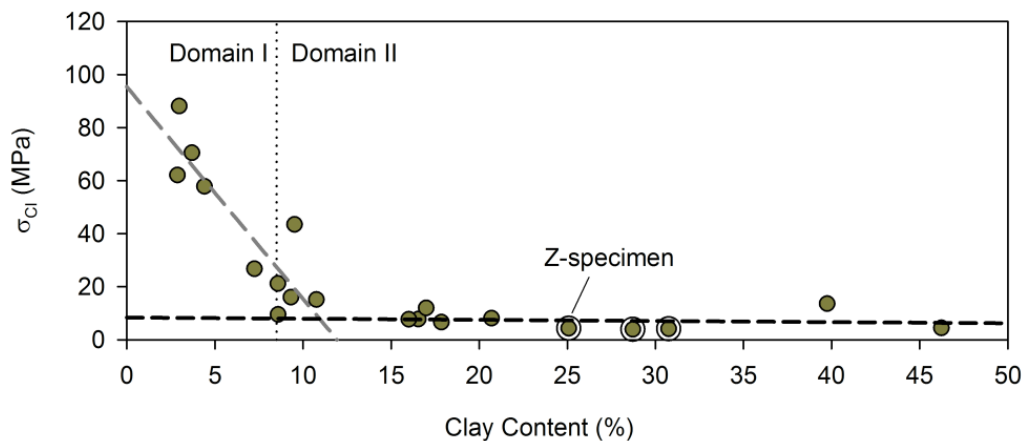
Figure 3.11 Relationship between total content of clay minerals and crack initiation stress (σ_{CI}); Z-specimens are shown with double circle. The crack initiation data were determined according to Method I [14].

The results of the compressive strength tests also suggest that σ_{CI} is not dependent on the specimen geometry (e.g. P, F, Z) when the clay content exceeds approximately 7-10%.
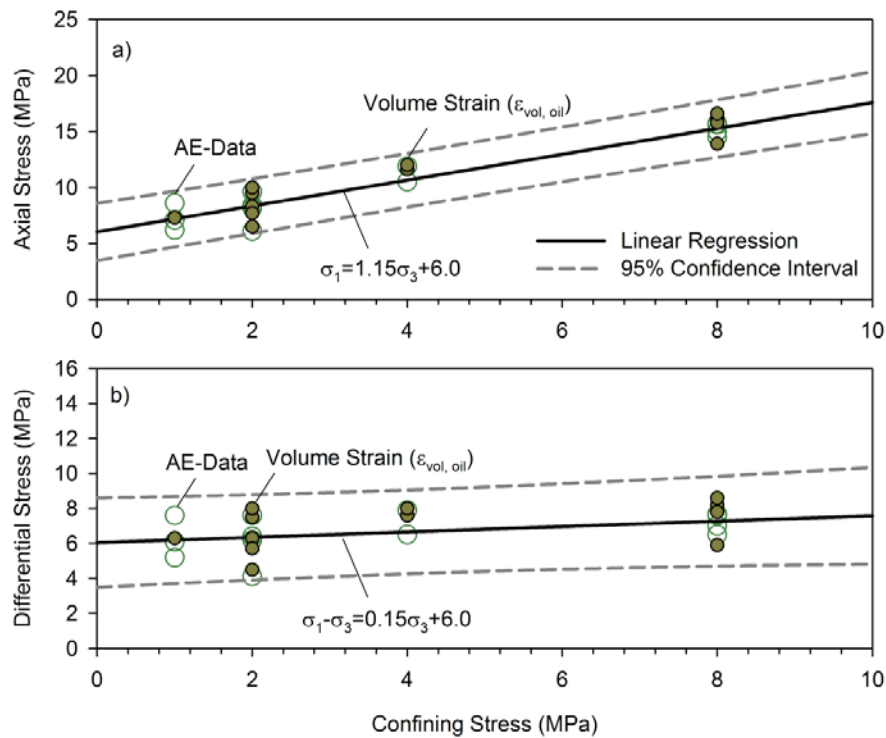
Figure 3.12 Stresses at the onset of dilatancy in triaxial compression: a) principal stress diagram; b) differential stress versus confining stress. Both, crack initiation obtained from micro-acoustic emission (AE) monitoring and the volumetric strain response ($\varepsilon_{vol, oil}$) are shown.

3.1.4 Heterogeneities and their influence on crack initiation and fracture growth

A series of thin sections obtained from representative specimens utilized for unconfined compressive strength tests were analyzed to investigate variations in σ_{CI} and fracture growth associated with micro-structural and mineralogical variations of the clayey matrix and heterogeneities such as Anhydrite veins. As outlined previously the clay matrix appears macroscopically homogeneous. The microscopic analyses of the clayey matrix revealed, however, distinct differences in the micro-structure and mineralogical composition of the clayey matrix. The dark grey to almost black clayey matrix in Figure 3.13a and b predominately consists of clay minerals with pervasively distributed fine-grained Anhydrite nodules or veins (white) on the sub-mm scale. The light grey matrix type in Figure 3.13a and b is made up of fine-grained clay and homogeneous distributed fine-grained Anhydrite minerals (called anhydrite-rich matrix). In general the Anhydrite content and distribution in the clayey matrix varies, and different matrix types usually co-exist in one specimen.
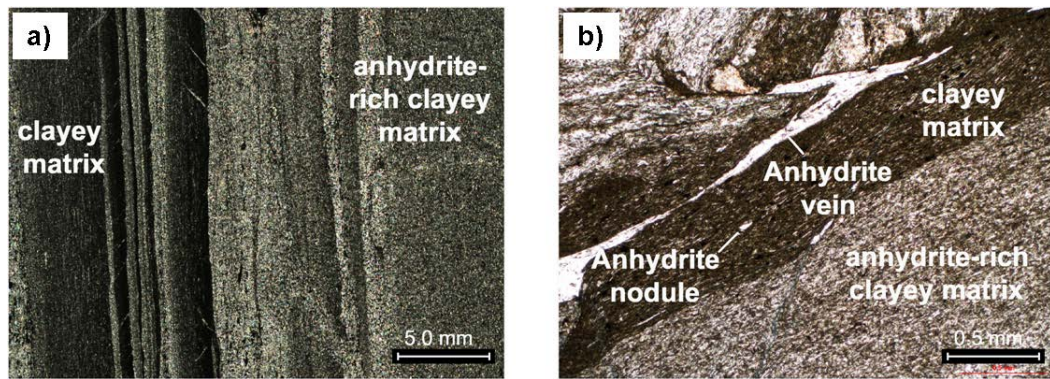
Figure 3.13 Typical thin section obtained showing variations in mineralogi-cal composition and micro-structure of the clayey matrix.

Klinkenberg et al. [43] reported similar observations for Tournemire Shale. They analyzed the influence of the micro-structure and mineralogical com-position on the strength of this shale, and showed that carbonate was ho-mogeneously distributed in the clayey matrix. With increasing carbonate content, the strength of this shale increased. Klinkenberg et al. [43] con-cluded that the increase in strength of the shale is associated with an in-creasing strength of the clayey matrix when the carbonate content in-creases. Based on the observations in this study, and the findings of [43], it is suggested here that variations in the magnitude of σ_{CI} are related to mi-cro-structural and mineralogical differences of the clayey matrix. In Domain II, the little scatter in σ_{CI} indicates that microcracks are initiated in a clayey matrix with similar strength properties. The increase of σ_{CI} in Domain I (Fig-ure 3.11) is interpreted to be related to an increasing Anhydrite content and thus strength of the clayey matrix. The occurrence of different clayey matrix types, and the transition to clayey matrix types with increasing Anhydrite content in Domain I might also explain the variability in σ_{CI} in the transition zone between Domains I and II. Specimens which contain few zones with lower-strength clayey matrix in between a predominately higher-strength clayey matrix (anhydrite-rich matrix) can show a low σ_{CI} value, although the total content of Anhydrite is relatively high.

As outlined in the previous section, σ_{CI} of specimens with an unconfined compressive strength larger than approximately 75 MPa (H-specimens) in-creases slightly at a rate of 3:10 (Figure 3.10). These specimens show a substantial different fabric compared to specimens in Domain II and the transition zone. Distinct layers of clay rock cannot be found and the speci-mens appear macroscopically homogeneous. The σ_{CI} obtained from these specimens is therefore only representative for homogeneous Anhydrite lay-ers in the Gipskeuper formation.

Figure 3.14a and b show typical thin sections from specimen used for un-confined compressive strength tests. Several microcracks can be seen in the clayey matrix. The microcracks are often oriented sub-parallel to the principal load direction (as indicated by arrows in Figure 3.14), and tend to open normal to the plane of the cracks. It was also observed for example in Figure 3.14b that the orientation of microcracks is variable and often inclined

or oblique to the loading axis, probably due to micro-structural or mineralogical variations (e.g. preferred orientation of clay minerals or distribution and mass fraction of fine-grained Anhydrite). As shown in Figure 3.14a and b, microcracks get arrested at the interface from clay rock to heterogeneities such as Anhydrite layers, veins or nodules. Figure 3.14 a and b also show microcracks alongside the interface between the clay matrix and the heterogeneity (called interface cracks). Interface cracks typically form alongside of Anhydrite veins or nodules (Figure 3.14b) or, as shown in Figure 3.14a, alongside anhydrite-rich clayey matrix zones. The latter observation supports the assumption that the anhydrite-rich clayey matrix has a higher strength and stiffness than the clay-rich matrix.
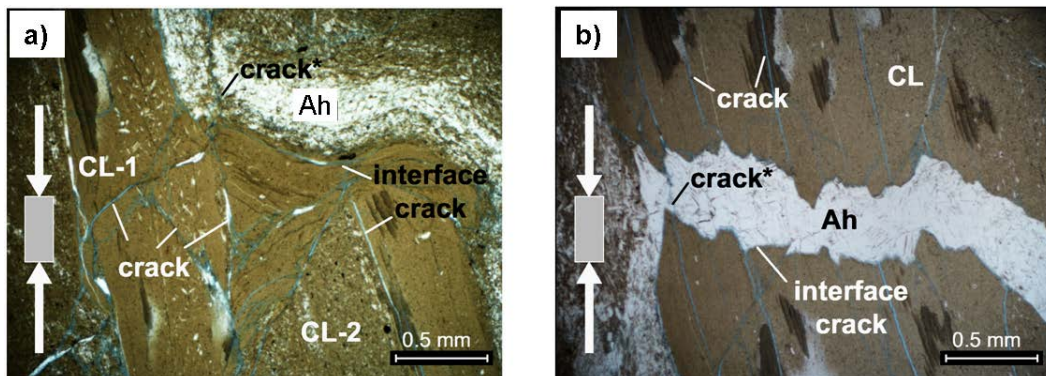
Figure 3.14   Thin sections prepared from specimens after compressive loading. The load axis is indicated by arrows. Ah: Anhydrite, CL: Clayey matrix, crack*: crack which penetrates Anhydrite veins or anhydrite-rich zone. CL-1 and CL-2 indicate micro-structural and mineralogical variations in the clayey matrix. CL-2 is characterized by continuous distributed anhydrite; the anhydrite content in CL-2 is higher than in CL-1.

The analyses of several thin sections revealed that the majority of the observed microcracks is distributed in the clayey matrix or follows an interface between the clayey matrix and heterogeneities. Interface cracks often link with micro-cracked clay layer forming an interconnected fracture network. Microcracks also penetrate Anhydrite veins as shown in Figure 3.14a and b. Such microcracks typically link micro-fractured clayey layers where the fabric of the rock prohibits linking through interface cracks, or when a clay nodule is surrounded by Anhydrite. Since Anhydrite veins are stronger than the clayey matrix, it is assumed that microcracks penetrating veins may have formed at higher axial stress levels than interface cracks.

As mentioned above, microcracks in the clayey matrix often tend to open normal to the principal load direction. Under laterally unconfined conditions, this process, together with shearing along oblique microcracks, is associated with an increase in the radial strain. Figure 3.15 shows the relationship between the axial and the radial strain in the pre-failure range for a typical heterogeneous specimen as the axial stress is increased.
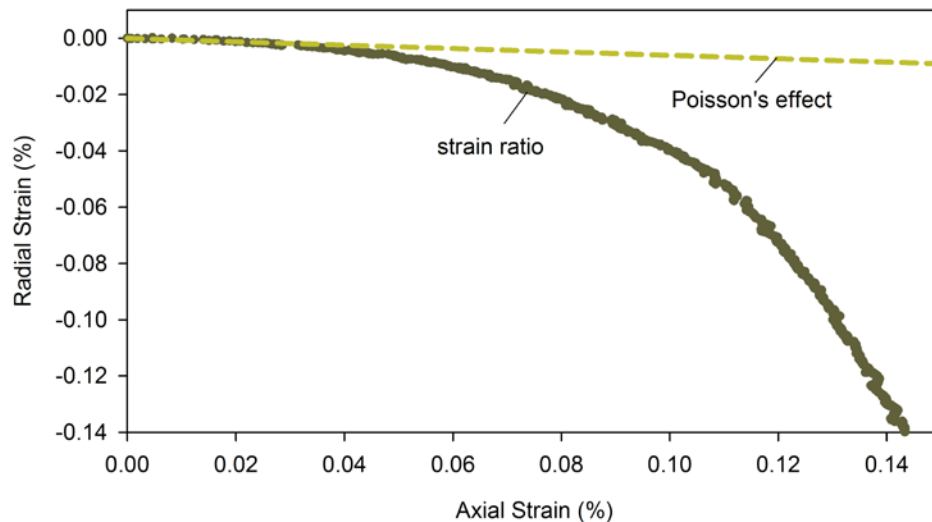
Figure 3.15 Axial strain versus radial strain typically observed in the pre-failure range during unconfined compression tests (specimen No. B3 318 is shown here) on specimens with a heterogeneous rock fabric (Domain II and transition between Domains I and II, Figure 3.11)

At low axial strain the curve corresponds to an elastic response, following the Poisson's effect. However, with increasing axial strain, at about 0.04% in this case, the radial strain increases disproportional to the axial strain indicating an ever increasing growth of extensional axial cracks. This disproportional increase often leads to an extensional macroscopic fracture (defined as fractures with a length on the cm-scale which are visible by naked eye) aligned with the maximum principal stress axis. Under laterally unconfined conditions such macroscopic axial fractures are usually visible in brittle rock types when the axial stress exceeds the crack damage threshold where a critical crack density is reached [19], [22]. However, it was observed in this study, that for sulfate-rich rocks, the majority of specimens do not show macroscopic cracks prior to or at failure (peak strength). Some specimens did not show macroscopic fractures even after intense post-failure straining (to as much as -0.5% radial strain). Only specimens with homogeneous fabric (clay content <5%) showed macroscopic cracking prior to failure. This observation, together with the observations from microscopic investigation suggests that microcracks forming under unconfined compression in heterogeneous specimens do not localize or form a macroscopic fracture prior to failure. This process is most probably controlled by the quantity, orientation and distribution of stiff heterogeneities which tend to arrest growing microcracks. Unstable crack growth in the pre-failure range, as typically observed in other brittle rock types ([19], [22] and many others), may therefore be less probable in specimens with a heterogeneous rock fabric with considerable stiffness or strength heterogeneities.

The heterogeneous rock fabric and micro-structure may also explain the sudden, distinct stress drops observed at different axial stress levels (Figure 3.16b). Note that a constant circumferential displacement rate was utilized as the controlling feedback signal for these unconfined compression tests. Therefore, stress drops are associated with the tendency of a sudden in-

crease of the radial strain as a consequence of microcrack initiation or propagation. Figure 3.16 shows the stress-strain behavior representative for specimens in Domain I (Figure 3.16a) and the transition zone between Domain I and II (Figure 3.16b).
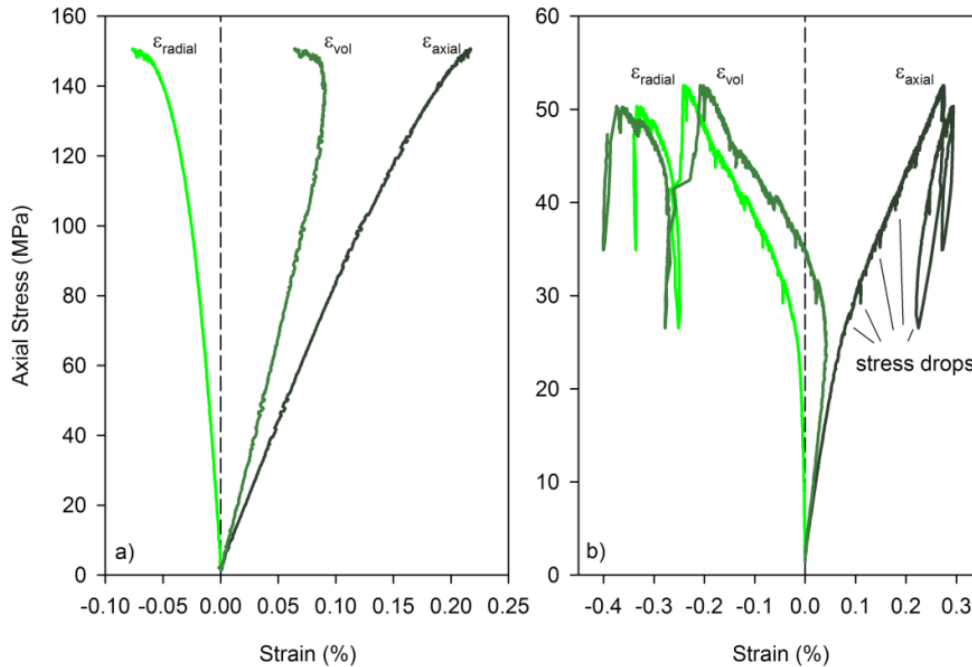
Figure 3.16 Stress-Strain response typical for specimen with a) homogeneous rock fabric (Domain I), and b) heterogeneous rock fabric with distinct clay layers and stiff heterogeneities (Domain II and transition between Domain I and II)

Specimens in Domain I, with no discrete clay layers, do not show considerable stress drops, whereas specimen in the transition zone (and in Domain II) characterized by a rock fabric consisting of distinct layers of clay rock with Anhydrite veins, exhibited several considerable stress drops of various magnitudes in the pre-peak and post-peak region (Figure 3.16b).

Micro-acoustic signals monitored during several triaxial compressive strength tests revealed a step-wise increase in acoustic emission counts with increasing differential stress, rather than a continuous increase as typically observed on other brittle rock types [41], [44]. This is illustrated by Figure 3.17 showing at least five steps and plateaus of reduced count rate increases at different differential stress levels.

The reasons for the stress-drops and step-wise increase in acoustic emissions with increasing differential loading are interpreted as being related to the heterogeneities (heterogeneous rock fabric and micro-structural variations in the clay matrix). As outlined in the previous section, different clay matrix types co-exist in a specimen. Each stress drop is interpreted as an indication of cracking of spatially distributed clayey matrix zones with different strength properties. In addition to the variability in the strength of the clayey matrix, it is reasonable to assume that the heterogeneous rock fabric creates stress and strain heterogeneities. As a consequence, the stress or

strain threshold required to initiate microcracks is eventually exceeded locally while other regions of the specimens still respond elastically to loading. Stiff heterogeneities may also experience less straining compared to clay layers were micro-fracturing is initiated at lower stress levels. The resulting strain differential can induce shear or tensile stresses at the interfaces, and ultimately lead to the formation of interface cracks. Sudden stress drops at higher stress levels could also be related to cracking of Anhydrite veins or the formation of interface cracks. In the post-peak range, these stress drops are often considerably larger (Figure 3.16b). It is assumed that the majority of these stress drops are associated with crack penetrating Anhydrite veins or the formation of larger interface cracks.
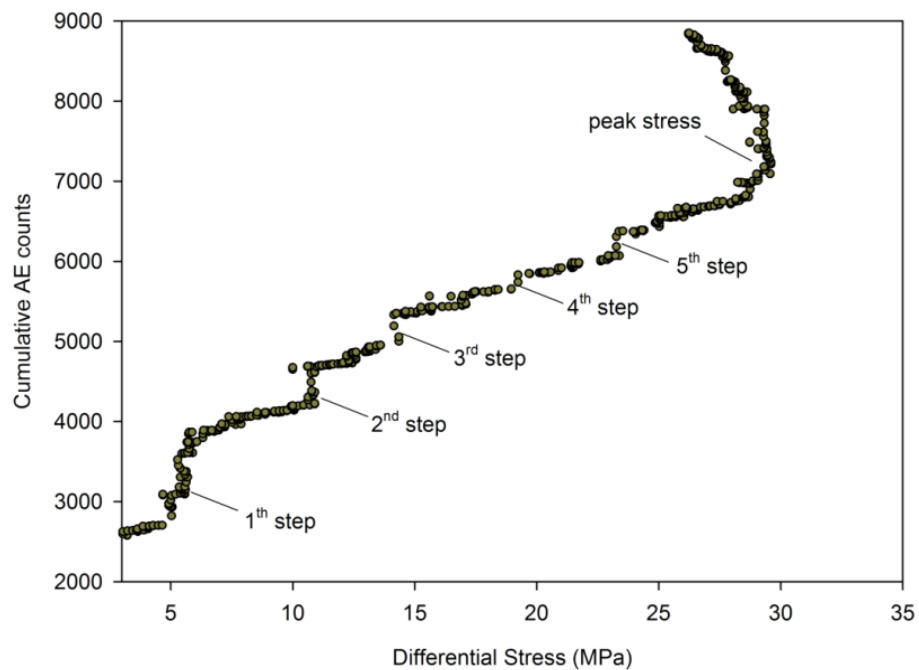
Figure 3.17 Discontinuous step-wise increase of acoustic emission events often observed during triaxial compression tests on specimens with a heterogeneous rock fabric

Major stress-drops in the pre-peak region were rarely observed in the stress-strain response obtained from triaxial tests (Figure 3.18 two of three shown cases show a distinct stress-drop in the pre-failure region). In addition, the majority of stress drops observed during triaxial compression tests occurred when the confining stress was low (e.g. ≤2 MPa). At higher confining stresses stress drops were rarely observed for tests on F- and P-specimens (e.g. specimen B 3 455; Figure 3.18), but systematically on Z-specimens. The difference in stress drops frequency in the pre-failure range between unconfined and confined compression tests is most likely associated with the chosen controlling feedback signal used for triaxial testing (constant axial displacement rate). The tendency for sudden changes in radial displacement due to extensional axial microcracks does not trigger any machine response when the pre-defined axial displacement rate can be maintained with the actual load increase. This suggests that the numerous stress-drops observed in unconfined compression tests are predominately associated with extensional fractures which are aligned with the principal

load axis. Stress drops during axial displacement controlled triaxial tests might indicate the formation or activation of shearing along oblique fractures.
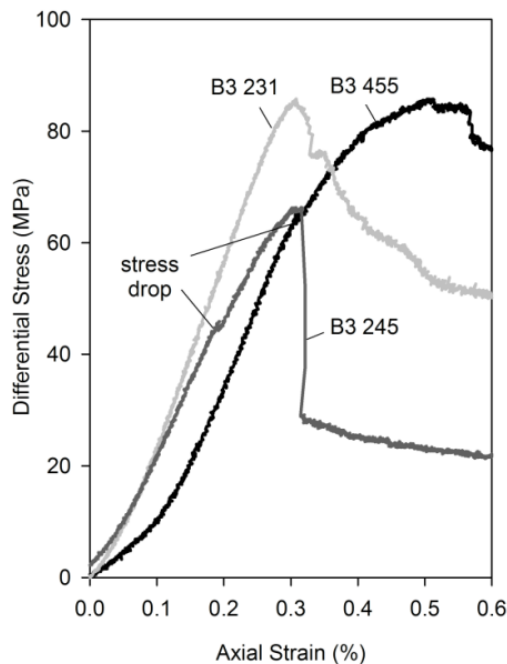
Figure 3.18 Stress – axial strain response of selected triaxial specimens. Distinct stress-drops can be seen in the stress – axial strain response of specimen B3 455 and B3 245.

3.1.5 Peak strength

From the discussion on the influence of heterogeneities on fracture formation and growth in the previous chapter it becomes evident, that with decreasing clay content (and therefore increasing Anhydrite vein density) the strength must increase. Figure 3.19 relates the unconfined compressive strength to the clay content. When the clay content exceeds 10-15% the unconfined compressive strength tends to decrease from approximately 20 to 5 MPa with increasing clay content. For a clay content >20% the specimen geometry (e.g. P- or Z-specimen) is of minor relevance for the unconfined compressive strength. For clay mineral content smaller 10-15% the UCS increases substantially with decreasing clay content from approximately 30 MPa to 150 MPa.

The results suggest that the peak strength of specimens with a heterogeneous rock fabric is to a considerable extent related to the Anhydrite content (Figure 3.19). The likelihood for growing microcracks to arrest at Anhydrite veins is associated with the vein density and the orientation of veins in respect to the fracture propagation direction. With increasing vein density, individual cracks or micro-fractured zones cannot coalescence at low axial loads, and fractures ultimately have to propagate through stiff veins.
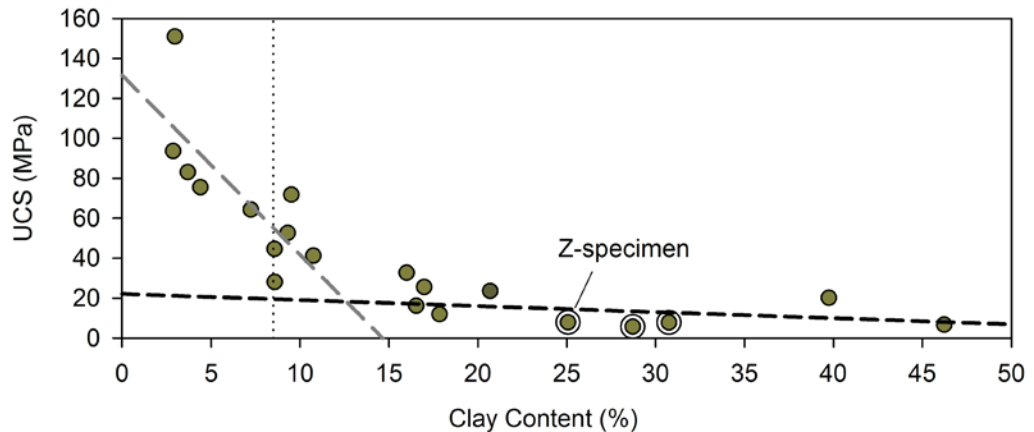
Figure 3.19 Relationship between total content of clay minerals and uncon-fined compressive strength (UCS); Z-specimens are shown with double cir-cle.

Specimens utilized for triaxial tests covered clay mineral content between 6.7 and 33.8 %, and the peak strength values, as illustrated by Figure 3.20 consequently show considerable scatter (note that σ_{CI} was almost constant for the same specimens). Depending on the mineralogical composition and failure mechanism (i.e., failure pre-dominantly through the clayey matrix), three groups with similar mineralogical composition, strength and failure characteristics could be identified (Figure 3.20). For the first group (Group I) results obtained from Z-specimen are combined with results from speci-mens with a clay content >20%, where specimen failure is controlled by the clayey matrix. Results from unconfined compressive strength tests on spec-imens with the most unfavorable orientation of bedding planes with respect to the loading axis showed exceptional low strength and were not consid-ered. Specimens in the second group (Group II) are characterized by clay content between 8.5 and 11.5% and folded (F-specimen) or discontinuous layers of Anhydrite veins oriented parallel to the loading axis (P-Specimen with discontinuous Anhydrite veins). Specimens in the third group (Group III) have clay content between 6.7 and 9.5% and continuous Anhydrite lay-ers oriented parallel to the load axis (P-specimen).

The data points shown in Figure 3.20 suggest that the peak strength cannot be adequately described by a linear failure envelope. A bi-linear envelope was used to account for the rapid strength gain at lower confining stress. The amount of data obtained in this study is insufficient to establish a peak failure envelope for the three groups by statistical means. However, a peak strength failure envelope was established for the three groups by assuming that the friction angle (or slope in the principal stress diagram) of all speci-men groups is the same in the lower and the higher confining stress range. Data obtained from Z-specimens and specimens with high clay content at a confining stress range >1 MPa were used to estimate the friction angle for the higher confining stresses by least-square linear regression. The friction angle obtained is 33°. The apparent friction angle for lower confining stresses was established from Group II and Group III and revealed a con-sistent value of 68°. Figure 3.20 shows the three bi-linear failure envelopes for the three groups, assuming that the friction at high confinement (beyond

and assumed spalling limit $\sigma_1/\sigma_3 = 60$) is the same for all specimens groups.
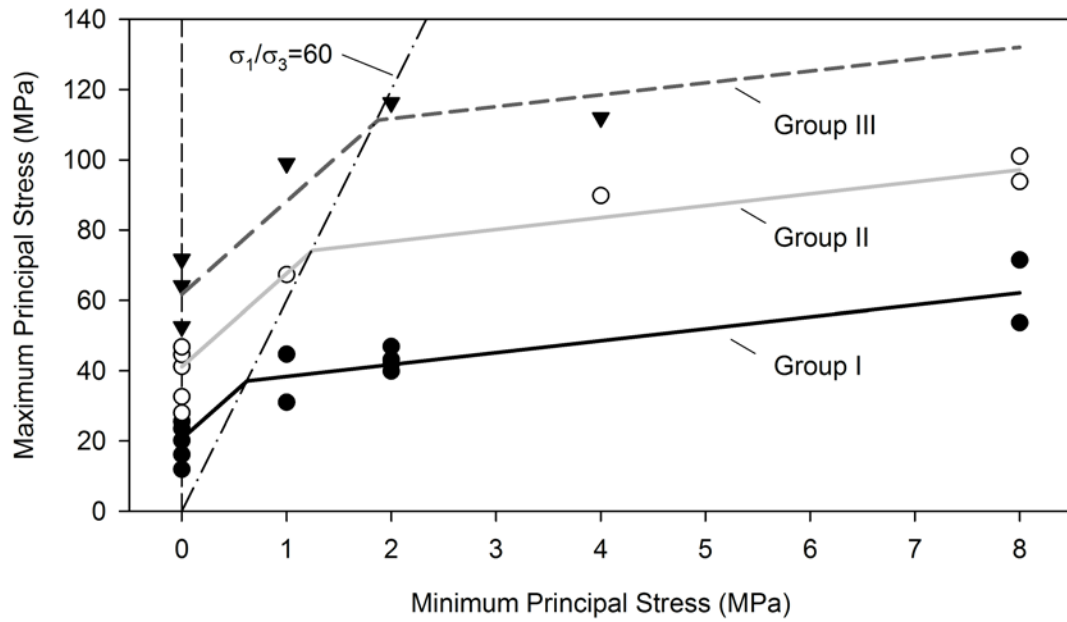
Figure 3.20 Peak-strength criterion for three groups of specimens with similar mineralogical composition and specimen geometry.

3.2   Analyses of borehole observations on the tunnel scale

3.2.1   Rock Mass Characterization

Rock Mass Fabric and Structures

The detailed analyses of cores and OPTV images, and XRD results were used to develop two geological cross sections (L1 and L2) below the invert of the Belchen Drainage tunnel as shown in Figure 3.21 and Figure 3.22. The layering and the geometry of the layers are based on 100 measurements of bedding plane orientations (Figure 3.23). It is assumed that the shown layering is a consequence of sedimentation processes. The clay content layering in Figure 3.21 and Figure 3.22 is based on 123 XRD analyses (sampling locations are shown in both Figures). Lateral variations might be a consequence of sedimentation and migration of sulfates in the tectonic history of the Gipskeuper formation. The present geological models are one possible interpretation but it is considered a most likely scenario.

The rock mass encountered in the six boreholes is macroscopically characterized by a heterogeneous rock mass fabric consisting of a sequence of clay rock and varying frequencies of Anhydrite veins or layers. The sequence is dominated by blackish gray clay rock with grayish white Anhydrite veins with a thickness ranging on the sub-mm- to cm- scale. Anhydrite-rich zones parallel to bedding were found in B3 at 3.4-4.1m, in B4 at 4.95-5.55m, and in B6 at 3.1-3.7m (Figure 3.21 and Figure 3.22). In addition to these anhydrite-rich zones, massive bedding parallel anhydrite layers with a thickness on the dm-scale were identified in B1 at 7.0-7.5 m, and B4 in 7.8-8.5m). Dolomite rich layers, which are typically encountered in the Gipskeuper formation [45] [46] were only observed in B1 at 7.95m and 8.1m, and below 9.1m in B4.

Bedding parallel Anhydrite veins and Anhydrite-rich layers generally show a continuous trace on the unwrapped OPTV image. The trace lengths of veins approximately normal to bedding (called bedding-normal veins) as shown in Figure 3.24 are typically relatively short and vary between 0.1 and 10cm. These veins were solely observed within clay-rich layers with few discrete bedding parallel Anhydrite veins. The latter often limit the trace length of bedding-normal veins on both ends (Figure 3.24).

In addition to variations in frequency, trace length and thickness of veins and layers, the orientation of bedding is associated with two macroscopic fold scales. One fold scale is characterized by an amplitude and wavelength on the m-scale, and the bedding plane orientations along the borehole axis could be established from the OPTV image (Figure 3.21, Figure 3.22 and Figure 3.23). The second, smaller scale fold scale showed amplitudes and wavelengths on the cm - scale. This small scale folding was limited to individual clay-rich zones that appeared intact on the OPTV images. However, core recovery in these zones was limited due to disintegration as a consequence of drilling and the relatively low strength of these layers.
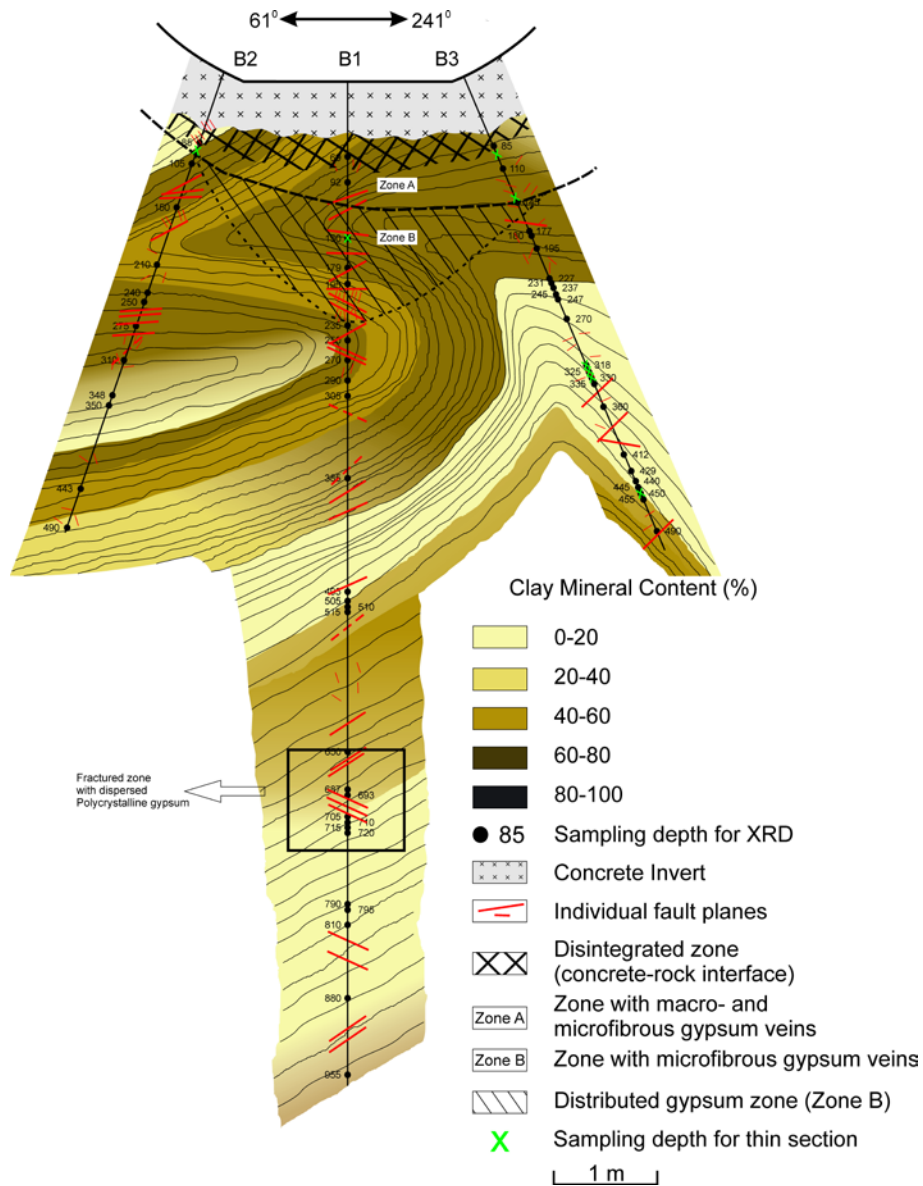
Figure 3.21 Geological Model in the cross-section L1 (Figure 2.3) and sampling locations for XRD analyses.
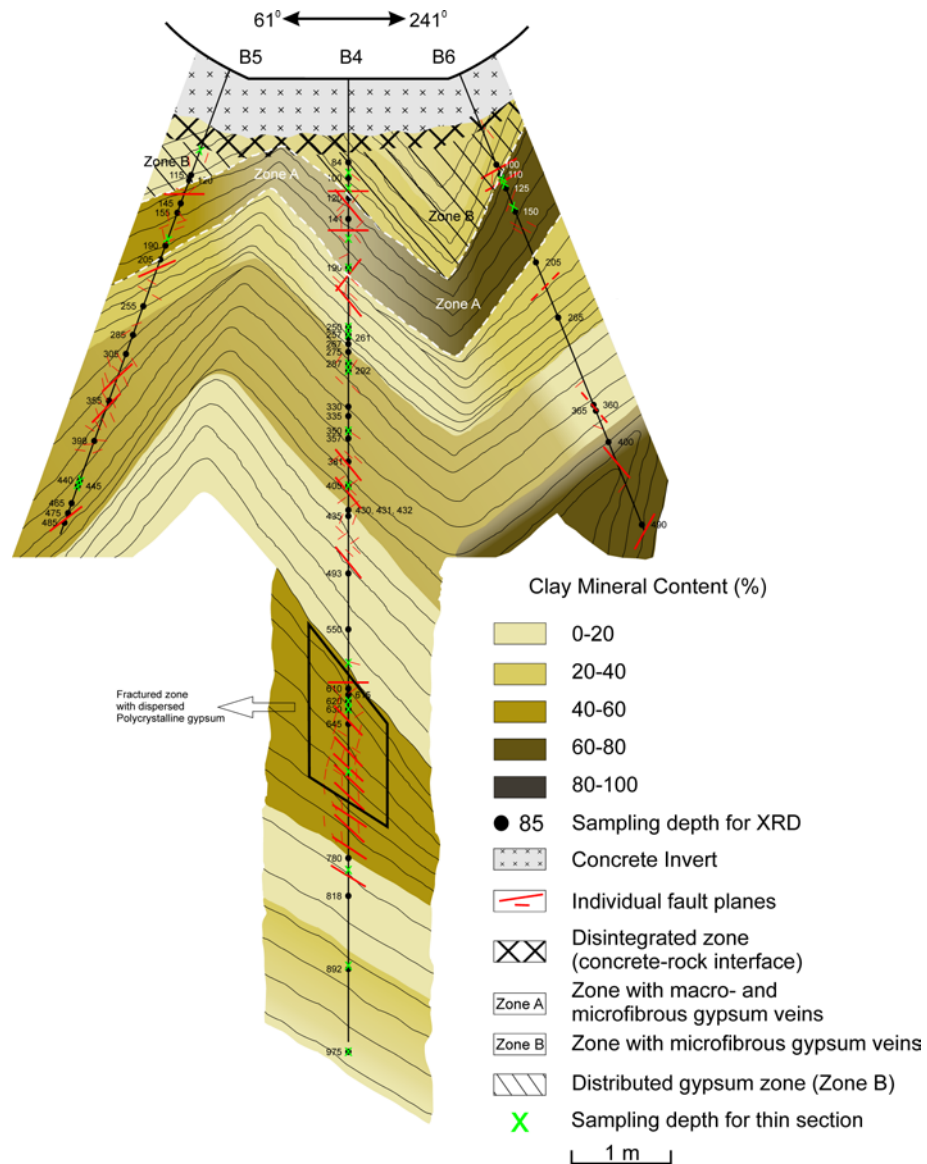
Figure 3.22 Geological Model in the cross-section L2 (Figure 2.3) and sampling locations for XRD analyses.

In addition to the above described structural features several individual discontinuities orientated unconformable to bedding were encountered (called randomly orientated veins in Figure 3.24). These discontinuities often show slickenside surfaces and were classified as fault planes. Fault planes are typically filled with anhydrite. Open discontinuities (e.g. not healed with fibrous gypsum or not filled with Anhydrite) were only observed in B6 at 0.7 and 0.8m. These open discontinuities are almost horizontal (e.g. the dip angle is approximately 0°) and unconformable to bedding (Figure 3.25).
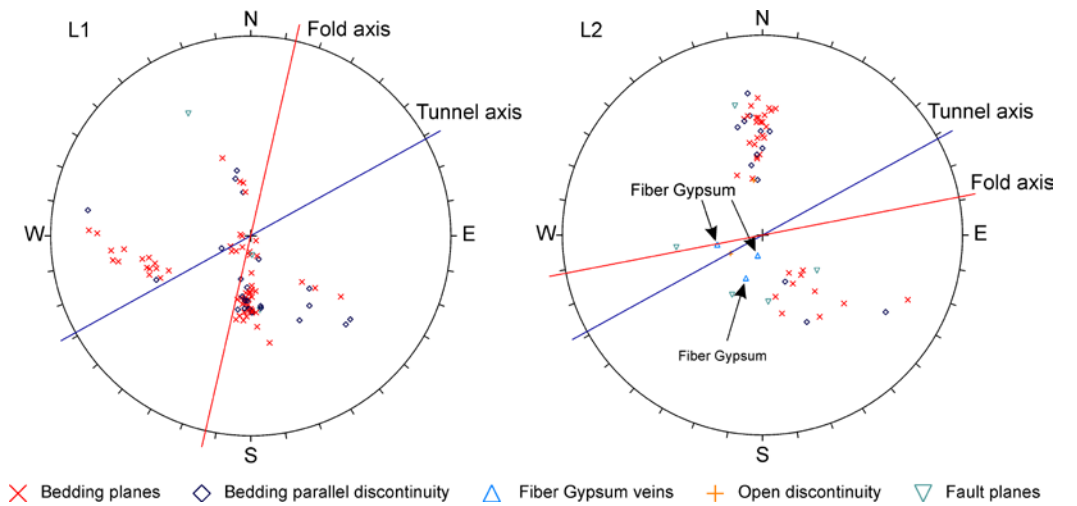
Figure 3.23 Orientations of measurable discontinuities obtained from OPTV images (Schmidt net; lower hemisphere)
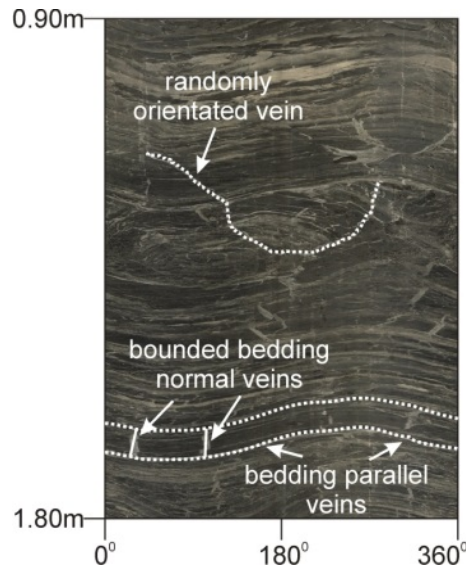
Figure 3.24 Section from the unwrapped OPTV image in B3 between 0.90m-1.80m. The figure shows bedding parallel Anhydrite veins, bedding normal Anhydrite veins, and a randomly oriented fibrous gypsum vein.
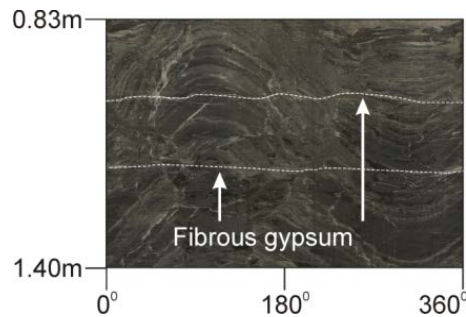
Figure 3.25 Unwrapped OPTV image of B6 between 0.83 and 1.4m showing two fibrous gypsum veins normal to the borehole axis. Note that B6 is 19° inclined in respect to vertical.

As mentioned above, the majority of discontinuities were filled with anhydrite, and was observed over the entire depth range of the six boreholes. However, several discontinuities with apertures on the sub-mm- to mm scale were healed with fibrous gypsum. These fiber-gypsum veins typically showed trace lengths on the cm-scale. The trace was often interrupted at Anhydrite veins in oblique angles to the fiber-gypsum veins. Due to the limited trace length and often irregular rather than planar trace, the orientation of these fiber-veins could not be determined with a sinusoidal fit on the unwrapped OPTV images (Figure 3.24). Even though, the image analyses showed that the orientation of these fiber-gypsum veins was primarily oblique to bedding. Only few slickenside fault planes or bedding parallel fractures were healed with fiber-gypsum. Three macroscopic fiber-gypsum filled discontinuities in B4 at a depth of 1.5m, and in B6 at depth of 1.0 and 1.17m, showed a planar trace, and a reasonable trace length for determining their orientations (Figure 3.23). The orientations (dip direction/dip) of these discontinuities were 14°/11° in B4, 21°/26° and 78°/26° in B6. The bedding orientations at these depths were on average 170°/55° in B4, and 345°/40° in B6.

The occurrence of macroscopic fiber-gypsum veins was limited to certain depth range below the tunnel invert as shown in Figure 3.21 and Figure 3.22 and summarized in Table 3.1. This zone is called Zone A (Figure 3.21 and Figure 3.22). Immediately beneath the concrete invert (concrete-rock interface), the rock mass was disintegrated in all boreholes and contained numerous randomly distributed and oriented fiber-gypsum veins. The thickness of these disintegrated zones was typically 0.1-0.3m (Figure 3.21 and Figure 3.22). In cross section L1 (Figure 3.21) fiber-gypsum veins were observed in the depth range between this disintegrated zone at the concrete-rock interface and a depth of 1.25m in B1, 0.95m in B2 and 1.6m in B3 (Figure 3.21 and Figure 3.22). In cross section L2 (Figure 3.22) macroscopic fiber-gypsum veins were only observed in a clay-rich layer beneath the tunnel as shown in Figure 3.22 (B4, from 1.1 to 1.9m, in B5, from 1.2 to 2.4m, and B6, from 1.0 to 1.9m). In the core sections above this clay-rich layer, the anhydrite content was substantially higher and characterized by several closely spaced anhydrite veins (e.g. high vein density).

3.2.2 Mineralogical Analyses

The sampling locations for the 123 XRD analyses are shown in Figure 3.21 and Figure 3.22; the mineralogical data are summarized in Appendix II.1. The ranges of the mass fractions of the mineral components analysed in this study are summarized in Table 3.1. Of particular interest for this study are the content of Anhydrite, Gypsum and Clay minerals (CM; i.e., the sum of the mass fractions of Smectite, Illite, and Chlorite). The depth distribution of these minerals along the axis is shown for borehole B1 in Figure 3.26, and for the remaining boreholes in Appendix II.1. The vertical dashed line in Figure 3.26 indicates the detection limit (0.5% mass fraction) for Gypsum in XRD analyses as suggested by [47]. The unwrapped image of the OPTV is shown in the background of these diagrams.

Overall, the mineralogical composition encountered in the six boreholes in

this study is dominated by the mass fractions of Anhydrite and Clay minerals, except in B1 at 7.95m and 8.1m, and below 9.1m in B4 where Dolomite was encountered.

Table 3.1 Ranges of mass fractions of major minerals analyzed in this study.

	Min (%)	Max (%)	Average (%)
Anhydrite	0.46	90.75	37.38
Gypsum	0	9.79	1.12
Total clay	2.69	79.87	32.25
Quartz	0	13.74	4.75
Magnesite	0	37.33	11.80
Dolomite	0	68.90	2.08
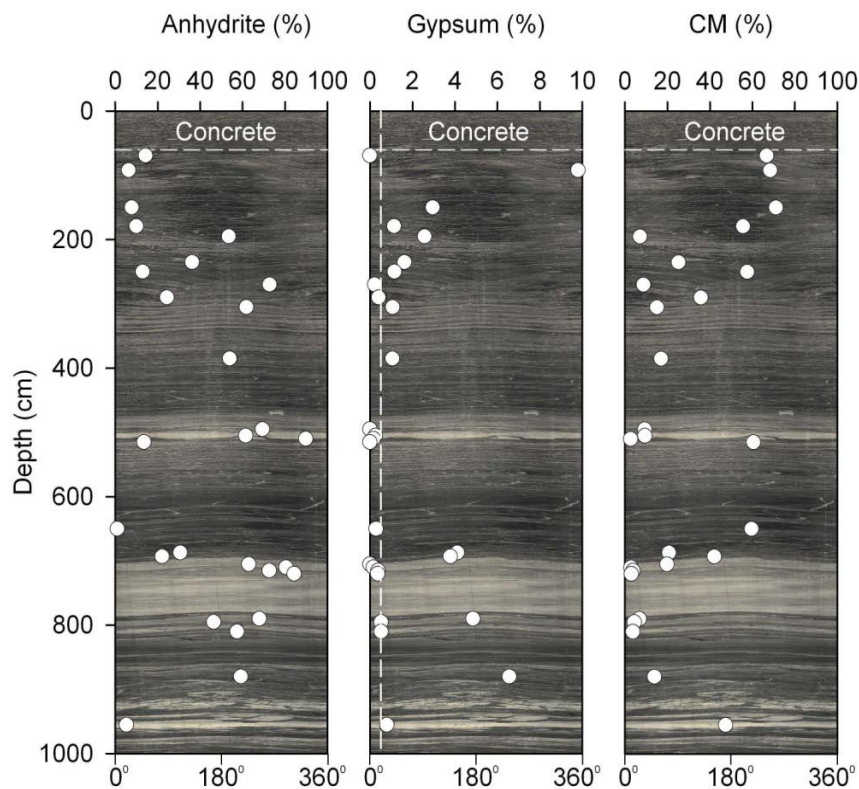
Figure 3.26 Depth distribution of Anhydrite, clay minerals and Gypsum in borehole B1. The unwrapped OPTV image of B1 is shown in the background. The vertical dashed line indicates the detection limits for Gypsum (0.5%) in XRD-analyses.

In Figure 3.26, the clay mineral and Anhydrite content vary strongly along the borehole axes. This is consistent with the heterogeneous rock mass fabric which is made up of discrete clay rock and Anhydrite veins, zones or layers. Although the distribution of clay minerals and Anhydrite is consistent with the heterogeneous rock mass fabric, the distribution of gypsum shows a general tendency in a zone of limited vertical depth between 0.60m (e.g. lower edge of the concrete invert) and maximum 2.35m below the tunnel invert (Figure 3.26). In this zone, significant Gypsum content was found to variable depth (Figure 3.21, Figure 3.22 and Figure 3.26) without any obvious relation to the macroscopic rock mass fabric or structures. The occur-

rence of Gypsum in this zone is consistent with the observation of macroscopic fiber-gypsum veins. However, in both cross section gypsum was also found in zones where no macroscopic fiber-gypsum veins could be identified. This is indicated in Figure 3.21 and Figure 3.22 as Zone B. At larger depth, Gypsum was found locally, primarily associated with the upper and lower edge of a massive anhydrite layer or anhydrite-rich zones (B1 at approximately 7.0m, 8.0m, and 9.0m; B5 at 4.8m), or in vicinity of individual fault planes (e.g. B6 at 4.9m, B4 at 6.1m). Note that the gypsum content in the six boreholes is relatively low and does not exceed 9.7% (B1 at 0.95m).

3.2.3   Microstructural Analyses

Orientated thin sections from various depths below the tunnel invert were analysed focusing on the micro-fabric, evidences for microcracks and mineralogy of micro-crack fillings. The sampling locations of these thin sections are shown in Figure 3.21 and Figure 3.22. All thin sections were oriented with the longitudinal axis parallel to the borehole axis as indicated by an arrow in Figure 3.27. This orientation allows determining the angle between discontinuities such as veins or microcracks and the borehole axis.

The micro-fabric obtained from several thin sections in this study revealed close similarities to the macro-fabric of the rock mass, and was characterized by a heterogeneous layered or folded sequence of clay layers and veins of multiple orientations (Figure 3.13). Veins mostly consist of crystalline Anhydrite (Figure 3.13 and Figure 3.14). Thin sections taken from Zone A and B (Figure 3.21 and Figure 3.22) showed fiber-gypsum veins with a width on the sub-mm-scale (Figure 3.27). These veins were only observed in the clay matrix. Most of these veins were entirely filled with fibrous gypsum with the longitudinal crystal axis almost perpendicular to the crack walls (Figure 3.27). Only occasionally it was observed that fibrous Gypsum was accompanied with crystalline Anhydrite (Figure 3.27d; photomicrograph on the left - parallel nicols, on the right crossed nicols).

In addition to these fiber-gypsum veins in the above mentioned zones, several open microcracks with an aperture on the sub-mm-scale were found (Figure 3.27). The occurrence of these open microcracks was limited to the clay matrix and the upper borehole meters (e.g. Zone A and B, Figure 3.21 and Figure 3.22). At larger depth, below Zone A and B, open microcracks were not observed in the thin sections.

An example of a series of open microcracks in the clay matrix is shown in Figure 3.28. From the distribution of fine-grained Anhydrite (dark grey to light grey color under parallel nicols, Figure 3.28) it can be seen that different clay matrix types co-exist. These differences are due to the mineralogical composition (e.g. Anhydrite content) and micro-structure (distribution of fine-grained Anhydrite). The orientation of the cracks in Figure 3.28 is overall perpendicular to the borehole axis. In the lower third of the thin section cracks alongside the interface between anhydrite-rich clay matrix and a clay matrix with less Anhydrite are visible.

The majority of open microcracks and fractures healed with Gypsum

showed a colored rim as illustrated in Figure 3.27a and b. These rims indicate alteration processes affecting approximately 0.05-0.1mm of the clay matrix, and are called alteration rims (Figure 3.27). Open microcracks with an alteration rim show that the crack walls are populated with gypsum crystals (Figure 3.27a, c).
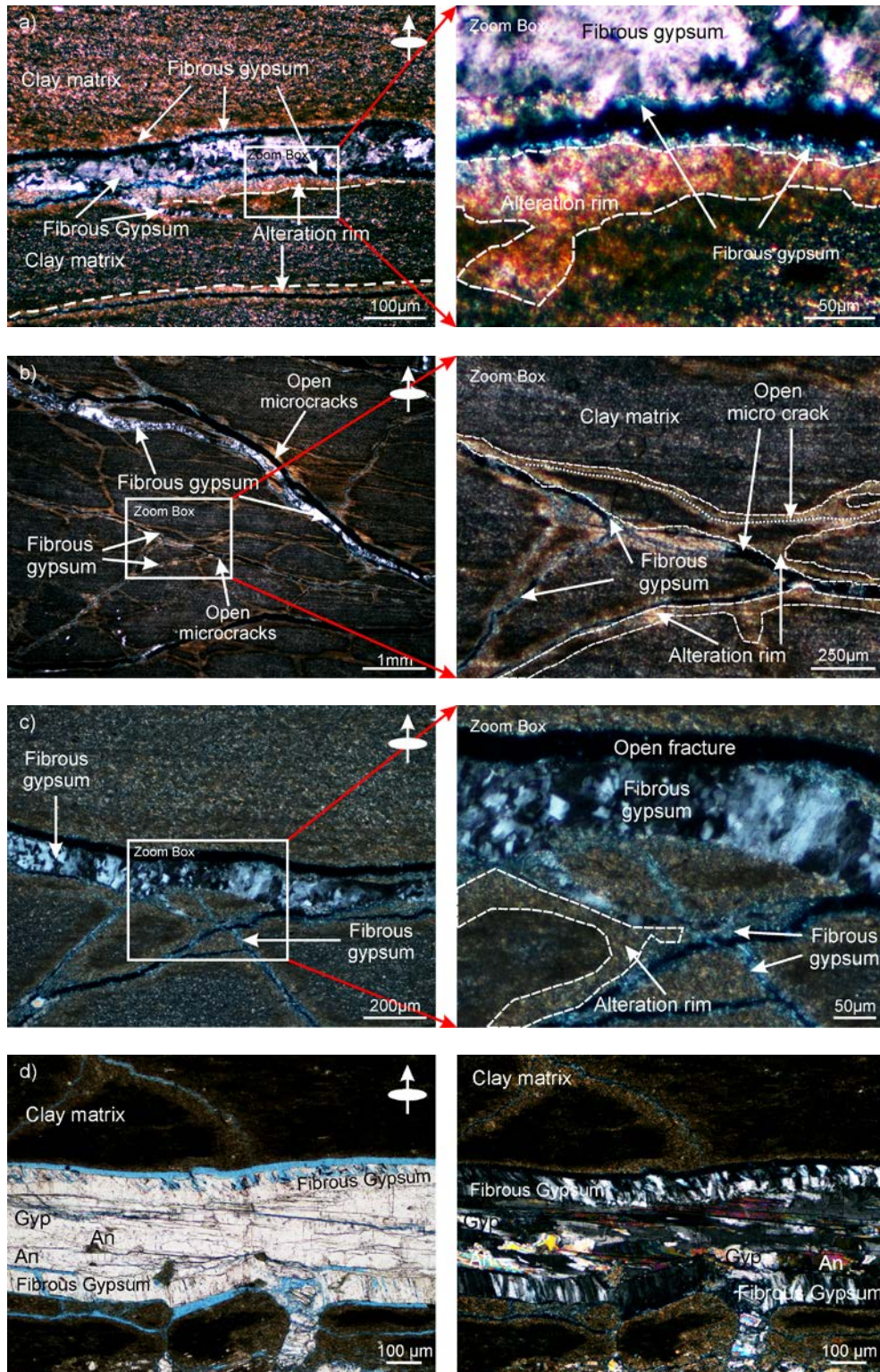
Figure continues on the next page.
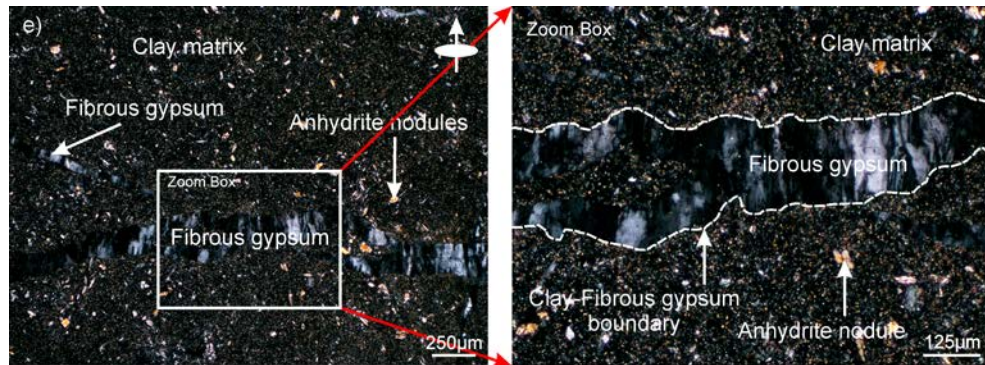
Figure 3.27 Photomicrographs of selected thin section obtained from samples within the first two meters below the invert of the Belchen Drainage Tunnel. The thin section show open and healed microcracks (fibrous Gypsum), and alteration rims alongside microcracks in the clayey matrix.
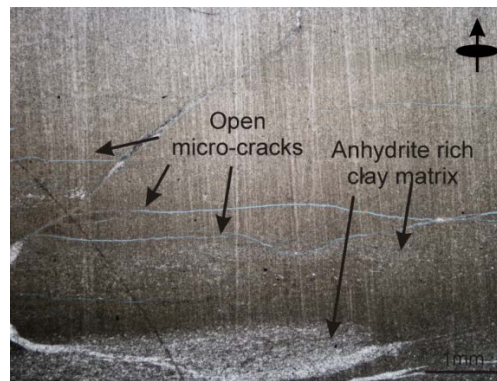
Figure 3.28 Example for open, unfilled microcracks in the clayey matrix. The thin section was obtained from a sample taken at a depth of 0.95m in Borehole B3. The figure shows open microcracks which formed in the clayey matrix and along the interface between clay matrix types of different mineralogical composition.
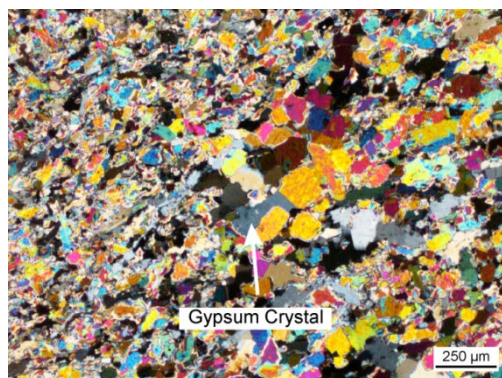
Figure 3.29 Crystalline gypsum within polycrystalline anhydrite at borehole depth > 2.5m

Occasionally it was observed, as shown in Figure 3.27, that gaps exist alongside fiber-gypsum veins. These gaps separate the crack walls form the core of the vein which is made up of fibrous gypsum. Figure 3.27 also shows that the crack walls are locally populated with Gypsum crystals. In other thin sections such as shown in Figure 3.27 fibrous gypsum crystals

are in tight contact to the crack walls, but co-exist with open, mainly oblique cracks with signs of initial gypsum precipitation.

The fibrous crystal structure of Gypsum observed in fractures in *Zone A and B* is substantially different to the crystal structure of Gypsum observed in thin section taken from larger depth below the tunnel invert. At this depth crystalline Gypsum appears randomly distributed within crystalline Anhydrite (Figure 3.29).

3.2.4 Interpretation

Secondary Gypsum

The analyses in this study showed that Gypsum exists in various depths below the tunnel invert of the Belchen Drainage Gallery. Gypsum at depth below 2.35m was solely crystalline and dispersed within Anhydrite veins (Figure 3.29). This is in contrast to the fiber-gypsum veins observed on the macro- and micro-scale within the first decimeters below the tunnel invert (Table 3.1). Madsen et al. [10], and Nüesch et al. [46] found that Gypsum which precipitated during swelling tests typically shows a fibrous structure. Such morphological properties of crystal structure are indicative for secondary crystal growth [10], and show substantial differences to gypsum crystals found at larger borehole depth. Crystalline gypsum may have formed under higher pressures and temperatures during the burial and tectonic history of the Gipskeuper formation [46]. It follows that the crystalline Gypsum found at a depth >2.35m below the Gallery invert is not related to the immediate influence of the tunnel. The fibrous Gypsum observed beneath the tunnel invert (to a maximum depth of 2.35m), however, is interpreted as newly formed Gypsum and thus related to tunneling.

Fracture distribution beneath the tunnel invert

The micro-structural and mineralogical analyses suggest two distinct zones beneath the tunnel invert: a Zone A, where the gypsum content was increased and macroscopic and microscopic fiber-gypsum veins co-exist, and a Zone B, where the gypsum content was increased and only microscopic fiber-veins exist. As shown in the cross sections L1 and L2 the depth ranges of these zones are limited to a finite depth below the tunnel invert (Figure 3.21 and Figure 3.22).

In the central part of cross section L1, Zone B reaches a substantially larger depth as Zone A. Observation in L1 suggests that the trace length of healed fractures beneath the tunnel invert decreases with increasing distance from the tunnel invert. In cross section L2 (Figure 3.22), Zone A is limited to a clay rich layer as shown in Figure 3.22 (e.g. clay content > 60%). Above this clay-rich zone the clay content is substantially lower and a high density of closely spaced Anhydrite veins exist (Figure 3.22 and Figure 3.26 see unwrapped OPTV image). Within this anhydrite-rich layer, fibrous Gypsum was only found in microcracks. As shown in the previous sections, propagating microcracks can get arrested at Anhydrite veins (depending on the orientation of Anhydrite veins in respect to the crack propagation direction). High deviatoric stresses are required to propagate microcracks through An-

hydrite veins, and thus the crack length is dependent on the stress magnitude and the amount, orientation and distribution of Anhydrite veins. The close spacing of veins in the anhydrite-rich layer above the clay-rich layer in L2 might explain that no macroscopic fractures can be observed, and Zone A is limited to the clay-rich layer. This is also consistent with the observation that in both cross sections the majority of healed macroscopic fractures showed a short trace length, and the trace often ended at Anhydrite veins.

The majority of the relatively short fractures were randomly orientated, but primarily oblique to bedding. Both, longer macro-fractures and the majority of micro-fractures observed in thin sections were almost perpendicular to the borehole axis and thus approximately tangential to the tunnel invert. The orientation of the majority of these fractures cannot be related to pre-existing discontinuity sets. Only few fiber-veins were found along slickenside fault planes or bedding parallel fractures. These finding indicates that only few pre-existing discontinuities opened or propagated as a consequence of tunneling induced stress relief. It is therefore concluded that the majority of the fiber-gypsum veins or open fractures below the tunnel invert were newly formed. However, opening of pre-existing discontinuities depends on the orientation of the discontinuity in respects to the stress orientation. In a geological situation other than observed in the two cross sections analyzed in this study, opening of pre-existing discontinuities might be more pronounced.

Fluid flow in fracture and fracture connectivity beneath the tunnel invert

The hydraulic conductivity and fracture connectivity beneath the Belchen Drainage Tunnel was not investigated in this study, and the influence of newly formed fractures on the hydraulic conductivity cannot be quantified. However, alteration rims along open and healed microcracks in the clay matrix (Figure 3.27) were found to a maximum depth of 2.35m beneath the tunnel invert. Fibrous gypsum was almost only found in these microcracks. Below 2.35m no microcracks or fibrous gypsum were found. Alteration of the clay matrix in close vicinity of microcracks is most probably related to fluid flow. These findings suggest that the observed microcracks in Zone A and Zone B serve as preferential pathways for water circulation and gypsum precipitation, and are most probably interconnected. It is assumed that fractures in Zone A and B may enhance the rock mass permeability, and fluid flow is primarily associated with the conductance and interconnection of these fractures.

Discussion of fracture origin

Most of the observed fractures healed with fibrous gypsum are newly formed fractures, show similar interconnected fracture networks as observed on specimens after mechanical loading, and, due to the proximity to the tunnel invert, are likely related to stress redistribution as a consequence of tunnel construction. The hypothesis advanced by Steiner et al. [38] and [39] of swelling potential induced or enhanced by brittle fracturing is consistent with observations presented in this report. However, the drainage tunnel is opened since 1999 and other time-dependent processes such as

rock mass degradation as a consequence of relative humidity and temperature cycling, or fracturing and fracture growth as a consequence of crystallization pressure at low confining stress beneath the tunnel invert [6] [8] will also have contributed to the current fracture network. From the analyses in this study, the time scales involved in the formation of the observed newly formed fractures and their gypsum infillings cannot be conclusively evaluated.

4   Conclusions

This study is based on in-situ observations and laboratory analyses of cores from 6 boreholes drilled into the invert of the Belchen Drainage Tunnel, Switzerland. The samples for these analyses were extracted from six boreholes drilled at the Belchen Drainage Tunnel in Switzerland in October 2011.

A series of unconfined and confined compression tests with acoustic emission monitoring, and microstructural and mineralogical analyses were used to investigate fracture formation in sulfate-rich clay rocks of the Gipskeuper formation. Core and optical televiewer logging, thin section and XRD analyses were used to characterize the rock mass at the tunnel scale in terms of mineralogical composition, discontinuity orientation, discontinuity infillings, and fracture network.

At the **laboratory scale** it was demonstrated that when the clay content is larger 7-10% microcracks in the clayey matrix are initiated under compressive loading conditions when the differential stress exceeds 4 to 13 MPa. For unconfined compressive strength tests the differential stress at crack initiation was 7 MPa on average, for triaxial tests 6 MPa. For a clay content > 7-10% the crack initiation threshold is independent of the confining stress, and for a clay content > 20% independent of the specimen geometry (e.g. loading axis in respect to the bedding plane orientation).

Crack propagation is influenced by Anhydrite veins. Depending on the Anhydrite vein density, distribution and orientation in respect to the crack propagation direction, growing microcracks may get arrested at Anhydrite veins. In case of a high vein density specimen failure requires high stresses or strains to link micro-fractured region either by interface cracks or by cracks which penetrate Anhydrite veins. This is seen as the primary cause for increasing strength with increasing Anhydrite vein density or decreasing clay content.

In addition to discrete Anhydrite veins, pervasively distributed fine grained Anhydrite exists and is seen as the primary cause of strength and stiffness variations in the clayey matrix. Upon compressive loading, both, Anhydrite veins and pervasively distributed fine grained Anhydrite may cause stress and strain heterogeneities and, as a consequence, localized failure processes at different strain or stress levels. This is supported by sudden stress-drops systematically observed in the stress-strain response obtained from unconfined compression tests, and the step-wise increase in acoustic emission counts during confined compression tests.

The majority of specimens showed neither prior to nor at peak strength macroscopic cracks. This observation suggests that upon compressive loading newly formed or growing microcracks cause distributed damage of the specimen but do not localize.

At the **tunnel scale** micro- and macrocracks healed with fibrous gypsum

were observed to a maximum depth of 2.35m below the tunnel invert. Fibrous Gypsum is related to the tunnel construction while Gypsum found at larger borehole depth showed a crystalline structure and may have formed during the burial and tectonic history of the Gipskeuper formation.

Micro- and macrocracks were only found in the upper decimeter to meter of the six boreholes. The majority of these cracks could not be related to pre-existing discontinuity sets, and are therefore considered as newly formed fractures. Only few fibrous Gypsum veins were found along bedding or fault planes in the first decimeters beneath the tunnel invert. Below a maximum depth of 2.35m neither open nor newly formed micro-/macrocracks were observed.

The majority of newly formed microcracks beneath the tunnel invert showed an alteration rim which penetrates approximately 0.05-0.1mm of the clayey matrix. Alteration rims are typically related to fluid flow. Fibrous gypsum was almost only found in these microcracks. These findings suggest that newly formed microcracks serve as preferential pathways for fluid circulation and gypsum precipitation, and are interconnected.

From the analyses in this study and the time scales involved, the rock mechanical processes underpinning the development of the observed newly formed fractures and their gypsum infillings cannot be evaluated. In addition to stress fracturing as a consequence of tunneling, time-dependent processes such as degradation or fracturing due to crystallization pressure may have contributed to the actual fracture network.

Appendix

Appendix

I   Rock mechanical laboratory results

I.1   Unconfined compressive strength tests

Table I.1.1   Results from unconfined compressive strength tests. Z: Z-specimen; P: P-specimen; F: F-specimen; H: specimen with a macroscopic homogeneous rock fabric; E: Young's Modulus; υ: Poisson's value; UCS: unconfined compressive strength; σ_{Cl} (I): crack initiation determined according to [14]; σ_{Cl} (II): crack initiation determined according to [20]; CM: mass fraction of clay minerals.

Bore-hole	Depth	Speci-men	E	υ	UCS	σ_{Cl} (I)	σ_{Cl} (II)	CM
(-)	(m)	(-)	(GPa)	(-)	(MPa)	(MPa)	(MPa)	(%)
B3	330	Z	2.8	0.13	5.6	4.0	3.8	28.72
B4	287	P	5.2	0.08	6.6	4.0	4.4	46.23
B4	630	Z	4.9	0.09	7.7	4.0	3.8	30.75
B3	335	Z	6.4	0.17	7.8	4.6	4.2	25.07
B3	318	F	6.1	0.09	11.9	6.6	6.4	17.85
B3	270	F	9.4	0.04	16.1	6.5	6.5	16.54
B3	445	P	42.2	0.16	20.1	15.2	12.9	39.74
B1	687	P	12.4	0.06	23.5	7.9	8.1	20.69
B1	385	F	29.7	0.19	25.5	12.4	12.1	16.98
B1	505	F	33.1	0.21	28	9.9	9.2	8.58
B5	485	P	35.3	0.07	32.6	10.5	7.7	16.07
B4	257	F	26.1	0.09	41.2	13.7	13.7	10.76
B3	412	P	65	0.18	44.6	22.1	22.4	8.57
B3	420	P	80.7	0	46.8	-	-	-
B1	495	F	36.1	0.11	52.6	17.4	13.4	9.31
B4	250	F	32.4	0.06	64.2	19.5	19.7	7.24
B3	450	P	68.8	0.16	71.7	45.5	40.0	9.52
B1	795	H	84.3	0.21	75.4	63.5	61.0	4.4
B1	810	H	77	0.21	83	72.5	63.5	3.69
B1	710	H	85.7	0.2	93.6	67.5	55.0	2.87
B1	720	H*)	80.2	0.21	150.9	89.5	85.5	2.97

P*) P-specimens with discontinuous stiff layers

I.2 Confined compressive strength tests

Table I.2.1 Results of the triaxial tests; Z: Z-specimen; P: P-specimen; F: F-specimen; E: Young's Modulus; υ: Poisson's value; σ_3: confining stress; σ_1, peak: peak strength; σ_{CI}, AE: Axial stress at crack initiation obtained from acoustic emission monitoring; σ_{CI}, vol: Axial stress at crack initiation obtained from volumetric strain response according to [14], CM: mass fraction of clay minerals.

Bore-hole	Depth	Specimen	E	υ	σ_3	$\sigma_{1, peak}$	$\sigma_{CI, AE}$	$\sigma_{CI, vol}$	CM
(-)	(cm)	(-)	(GPa)	(-)	(MPa)	(MPa)	(MPa)	(MPa)	(%)
B4	330	Z	14.5	0.14	8	71.5	15.0	13.9	10.94
B1	270	Z	12.1	0.30	2	39.9	8.2	8.3	9.33
B3	249	Z	24.2	0.10	2	46.9	8.4	9.5	13.72
B4	267	Z	5.4	0.31	1	44.7	8.6	-	9.21
B4	335	Z	22.3	0.37	1	31	6.2	-	13.31
B4	335	Z	10.1	0.30	2	42	6.1	6.5	13.31
B4	405	P	11.2	0.20	8	53.7	15.6	16.2	33.81
B3	440	P	12.3	0.07	2	43.2	-	7.7	20.4
B4	275	P*)	25.8	0.08	8	101	15.7	15.8	9.21
B3	455	F	29.9	0.31	8	93.8	14.5	16.6	11.49
B3	245	P*)	25.8	0.27	1	67.3	7.1	7.3	9.36
B3	231	F	32.1	0.10	4	89.8	10.5	11.6	9.87
B3	227	P	37.4	0.16	4	112	11.9	12.0	7.23
B5	505	P	64.9	0.19	2	116.3	9.6	10.0	6.7
B4	495	P	62	0.10	1	99	-	-	6.84

II Results of the mineralogical analyses

II.1 Quantitative XRD results obtained from Rietveld refinement

Table II.1.1 Quantitative XRD results obtained from Rietveld refinement B1

Depth	Anhydrite	Celestine	Chlorite	Dolomite	Gypsum	Illite	Magnesite	Muscovite	Orthoclase	Plagioclase	Pyrite	Quartz	Smectite	Total Clay
69	14.26	0.90	27.28	0.30	0.00	26.94	7.54	1.86	3.00	0.90	0.40	2.75	12.50	66.72
92	6.30	0.80	25.80	0.52	9.79	25.82	5.03	2.69	2.90	0.40	0.10	2.18	16.72	68.34
150	7.76	0.90	29.73	0.80	2.95	29.76	5.70	2.61	2.60	1.00	0.30	4.37	11.59	71.08
179	9.95	0.80	24.29	0.86	1.13	25.39	15.12	3.84	7.20	0.90	0.30	5.66	5.91	55.59
195	53.47	0.20	5.22	0.00	2.57	1.83	11.02	6.50	2.80	0.90	0.00	13.74	0.00	7.05
235	36.24	0.60	4.12	0.64	1.62	20.37	21.13	3.86	5.60	0.30	0.50	4.16	0.67	25.16
250	12.88	0.60	25.17	0.62	1.15	21.93	10.61	5.45	4.50	0.40	0.40	3.93	10.47	57.57
270	72.71	0.00	2.27	0.24	0.22	6.45	7.29	2.37	1.20	0.00	0.20	3.06	0.00	8.72
290	24.38	0.70	5.01	0.00	0.40	25.72	20.51	5.07	7.70	0.60	0.60	4.19	4.96	35.69
305	61.77	0.20	4.70	0.00	1.06	7.06	5.48	3.26	2.60	0.80	0.70	7.94	3.28	15.04
385	53.89	0.40	4.51	0.00	1.05	9.27	10.21	4.01	3.60	0.80	0.70	6.96	3.20	16.98
495	69.30	0.20	3.34	0.00	0.00	5.97	11.56	2.44	2.50	0.20	0.70	2.03	0.00	9.31
505	61.44	1.10	2.32	0.20	0.26	7.01	18.85	2.39	2.00	0.30	0.90	2.17	0.00	9.33
510	89.71	1.30	2.23	0.27	0.16	0.46	0.13	0.00	1.30	1.40	0.30	0.00	0.00	2.69
515	13.51	0.80	29.80	0.41	0.00	19.39	11.16	3.75	4.30	0.20	0.60	3.65	11.33	60.52
650	0.95	0.80	30.30	0.14	0.28	20.36	25.79	4.21	4.30	0.20	0.40	3.20	8.89	59.55
687	30.62	0.40	5.36	0.20	4.11	14.38	25.58	4.36	3.70	0.40	0.80	9.08	0.95	20.69
693	22.06	0.50	21.39	0.94	3.78	13.85	18.17	3.32	3.10	0.00	0.50	4.47	6.81	42.05
705	62.85	0.30	3.22	0.12	0.00	16.55	7.64	2.39	3.30	0.20	0.40	2.63	0.00	19.77
710	80.41	0.20	2.29	12.29	0.16	0.58	0.13	0.00	0.80	0.50	0.40	0.48	0.00	2.87
715	72.52	0.30	3.05	18.14	0.38	0.73	0.16	0.00	0.50	1.20	0.40	0.75	0.00	3.78
720	84.23	0.40	2.05	7.84	0.36	0.92	0.12	0.00	0.50	1.20	0.30	0.26	0.00	2.97
790	67.84	0.30	2.06	10.29	4.85	4.66	0.19	1.03	2.50	0.40	0.50	4.30	0.00	6.72
795	46.35	0.17	2.36	43.87	0.52	2.04	0.05	0.00	0.19	0.19	0.58	1.31	0.00	4.40
810	57.38	0.16	2.35	30.19	0.52	1.34	0.07	0.62	1.14	0.23	2.93	1.41	0.00	3.69
880	59.16	0.44	3.78	0.00	6.56	10.07	0.17	3.99	4.29	1.14	1.01	7.30	0.00	13.85
955	5.27	9.70	23.34	25.71	0.79	20.05	0.27	3.60	2.40	2.00	0.70	1.00	4.02	47.41

Table II.1.2 Quantitative XRD results obtained from Rietveld refinement B2

Depth	Anhydrite	Celestine	Chlorite	Dolomite	Gypsum	Illite	Magnesite	Muscovite	Orthoclase	Plagioclase	Pyrite	Quartz	Smectite	Total Clay
85	46.42	0.80	5.77	0.31	7.26	12.14	4.59	4.59	4.40	0.60	0.50	6.22	0.00	17.91
105	4.66	0.60	41.80	0.31	0.31	23.83	5.47	3.47	2.40	0.00	0.00	1.97	14.24	79.87
150	18.66	0.80	22.84	0.66	0.93	19.27	8.68	6.24	4.20	0.40	0.10	4.27	12.75	54.86
210	24.69	0.80	22.23	0.74	0.52	18.13	8.71	5.66	3.70	0.40	0.10	3.67	10.16	50.52
240	9.01	1.40	34.70	0.53	0.65	22.57	9.18	2.29	2.50	0.20	0.10	2.47	13.77	71.04
250	33.34	0.50	29.00	0.33	1.02	8.44	7.87	3.64	1.90	0.20	0.50	4.52	7.69	45.13
275	23.56	0.60	20.93	0.00	0.39	17.19	10.78	5.70	5.60	0.40	0.40	4.95	8.14	46.26
310	36.47	0.40	3.15	0.08	0.56	15.25	22.80	4.05	6.00	0.70	0.60	9.81	0.00	18.40
348	74.15	0.50	1.96	0.16	0.37	5.95	7.11	1.41	2.60	0.60	0.40	3.30	0.00	7.91
350	60.36	0.50	2.79	0.00	0.63	10.00	12.41	1.98	4.90	0.90	0.60	3.24	0.00	12.79
443	13.32	0.60	22.64	0.74	0.15	22.34	11.21	5.68	5.40	0.40	0.30	3.64	13.21	58.19
490	14.51	0.70	26.30	0.75	0.47	17.61	14.52	4.87	4.90	0.20	0.00	4.29	10.27	54.18

Table II.1.3 Quantitative XRD results obtained from Rietveld refinement B3

Depth	Anhydrite	Celestine	Chlorite	Dolomite	Gypsum	Illite	Magnesite	Muscovite	Orthoclase	Plagioclase	Pyrite	Quartz	Smectite	Total Clay
85	57.33	0.30	4.71	0.00	1.47	3.34	9.00	5.90	2.30	1.00	0.10	12.80	0.00	8.05
110	18.70	0.60	24.60	0.63	1.39	17.50	9.73	2.74	2.70	0.60	0.10	7.30	12.00	54.10
145	5.77	0.90	28.74	0.61	3.02	24.68	9.60	3.66	3.00	0.20	0.00	3.21	16.57	69.99
177	5.81	0.80	20.17	0.71	9.29	24.91	12.69	4.01	5.60	0.50	0.40	5.52	8.38	53.46
180	20.14	0.80	21.55	0.82	1.01	19.75	13.89	4.31	4.50	0.30	0.40	3.50	8.63	49.93
195	21.91	0.60	20.61	0.81	0.45	19.35	15.00	4.64	4.70	0.30	0.40	2.39	8.72	48.68
227	56.48	0.40	2.80	0.00	0.22	4.43	23.54	2.42	2.40	0.30	0.90	4.83	0.00	7.23
231	55.48	0.20	3.02	0.00	0.43	6.85	18.71	3.53	3.40	0.40	0.80	6.00	0.00	9.87
237	60.98	0.20	2.71	0.04	0.23	7.22	14.27	3.11	3.70	0.60	0.70	5.04	0.00	9.93
245	70.15	0.10	3.04	0.04	0.31	6.32	10.12	1.80	2.40	0.50	1.10	2.61	0.00	9.36
249	54.35	0.30	3.19	0.00	0.00	9.49	13.57	3.96	4.70	1.10	0.90	6.35	1.04	13.72
270	56.79	0.51	4.39	0.00	0.52	10.27	7.73	4.63	4.44	1.13	0.81	5.20	1.88	16.54
318	51.29	0.41	5.32	0.00	0.83	9.54	8.59	4.34	3.59	0.82	0.68	10.23	2.99	17.85
325	21.12	0.55	23.21	0.00	0.52	16.06	8.40	6.04	5.05	0.70	0.53	6.07	11.57	50.84
330	45.91	0.61	5.48	0.18	0.20	19.74	10.13	4.89	4.70	0.49	0.53	4.70	2.14	27.36
335	34.17	0.61	5.43	0.00	0.45	16.81	14.65	5.65	6.77	2.35	0.86	5.15	5.71	27.95
360	32.64	0.39	4.38	0.34	1.40	18.01	20.02	4.39	6.51	0.74	0.57	7.25	3.14	25.53
412	47.94	0.13	2.35	0.00	0.91	6.22	25.81	2.95	4.51	0.39	0.73	7.15	0.00	8.57
429	61.48	0.82	2.21	0.00	1.09	4.76	15.48	0.70	4.82	1.30	0.75	5.45	0.00	6.97
440	51.13	0.51	4.87	0.16	0.00	9.66	14.03	4.86	3.70	0.67	1.11	4.57	2.97	17.50
445	36.86	0.60	26.28	0.69	0.64	8.64	8.82	4.08	2.30	1.00	0.70	2.85	4.82	39.74
450	67.61	0.23	3.25	0.00	0.36	6.27	14.28	1.19	2.02	0.36	0.78	2.30	0.00	9.52
455	70.32	0.30	2.63	0.00	0.00	8.86	8.81	1.83	2.00	0.50	0.80	2.45	0.00	11.49
490	25.67	0.50	22.70	0.65	0.62	15.22	10.78	5.71	3.90	0.50	0.50	4.87	8.20	46.12

Table II.1.4   Quantitative XRD results obtained from Rietveld refinement B4.

Depth	Anhydrite	Celestine	Chlorite	Dolomite	Gypsum	Illite	Magnesite	Muscovite	Orthoclase	Plagioclase	Pyrite	Quartz	Smectite	Total Clay
84	49.92	0.20	5.54	0.00	1.31	5.42	7.90	5.65	3.30	0.90	0.00	13.07	5.51	16.47
100	31.20	0.70	3.63	0.00	0.55	15.35	26.62	6.05	4.10	0.50	0.30	8.37	2.50	21.48
120	26.12	0.50	27.81	0.52	0.76	11.19	15.71	3.84	3.40	0.30	0.20	5.84	3.61	42.61
141	20.97	0.60	21.72	0.61	0.10	19.14	10.48	4.55	2.80	0.50	0.20	5.48	11.30	52.16
190	20.53	0.60	21.12	0.45	0.24	18.83	11.06	5.41	5.00	0.50	0.60	3.35	10.88	50.83
250	70.49	0.14	2.08	0.00	0.22	5.16	10.89	2.18	2.60	0.60	0.60	3.57	0.00	7.24
257	58.94	0.29	2.67	0.00	0.44	7.96	14.55	2.93	3.43	0.55	0.65	6.13	0.13	10.76
261	64.69	0.50	2.98	0.00	0.00	5.63	14.35	2.38	2.80	0.60	0.30	4.08	0.00	8.61
267	67.02	0.20	2.00	0.00	0.34	7.21	10.85	1.94	2.60	0.60	0.60	5.31	0.00	9.21
275	42.59	0.60	4.23	0.00	0.00	19.55	15.37	4.28	6.60	0.20	0.60	3.74	1.96	25.74
287	20.28	0.66	20.32	0.68	0.63	15.21	15.91	5.41	5.52	0.43	0.55	3.49	10.70	46.23
292	40.54	0.61	3.08	0.28	0.00	20.30	17.01	4.65	6.39	0.46	0.66	4.66	1.11	24.49
330	71.73	0.32	3.30	0.22	0.27	8.43	5.72	1.20	2.58	0.62	0.64	3.21	0.00	11.73
335	63.08	0.30	4.02	0.00	0.52	8.40	7.01	2.89	3.50	0.60	0.70	5.67	2.02	14.44
350	29.20	0.70	23.37	0.46	0.80	11.66	8.76	3.67	4.00	1.40	0.60	3.83	9.63	44.66
350	30.80	0.60	23.31	0.62	0.32	13.57	9.18	5.68	4.50	0.30	0.50	4.31	5.70	42.58
357	51.80	0.80	5.36	0.11	0.21	11.47	11.17	5.89	4.40	1.10	0.60	5.47	0.33	17.16
381	9.81	1.10	23.03	0.51	0.00	28.59	11.12	2.43	5.10	1.40	0.50	3.56	11.40	63.02
405	20.23	0.50	20.26	0.70	0.49	17.05	16.03	4.40	5.10	0.40	0.60	5.82	8.14	45.45
430	13.50	1.00	5.36	0.19	0.33	24.12	33.06	4.73	7.70	1.00	0.20	5.87	2.96	32.44
431	31.81	0.60	4.29	0.18	0.35	21.67	19.19	4.79	6.40	0.50	0.70	6.15	3.18	29.14
432	50.07	0.60	3.89	0.09	0.30	12.29	13.34	4.21	4.20	1.00	0.80	5.60	1.49	17.67
435	6.90	1.40	18.78	0.67	0.00	28.06	23.90	2.22	5.60	0.50	0.30	4.60	6.49	53.33
493	45.25	0.40	3.48	0.00	1.59	7.13	22.27	2.85	5.10	0.60	0.90	5.72	3.41	14.02
550	59.02	0.40	3.83	0.00	0.88	10.20	13.33	2.12	3.20	0.50	0.90	1.08	0.00	14.03
610	24.87	0.70	23.11	0.97	0.00	16.04	10.61	5.38	3.80	0.50	0.50	2.84	9.26	48.41
615	32.29	0.60	28.10	1.17	0.98	9.02	9.48	3.91	3.40	0.90	0.30	3.81	4.98	42.10
620	11.73	1.20	32.40	0.52	0.99	20.81	9.87	4.14	3.70	0.30	0.40	3.00	9.62	62.83
630	26.85	0.30	19.98	1.50	7.33	16.16	7.23	3.96	3.40	0.30	0.50	5.06	6.20	42.34
645	20.10	0.60	26.00	0.78	2.52	19.96	7.23	2.37	4.20	0.40	0.60	6.09	8.96	54.92
780	80.38	0.40	3.14	0.89	0.00	5.39	1.90	1.17	2.40	0.60	0.50	0.96	0.00	8.53
818	90.75	0.40	1.84	0.77	0.37	1.19	0.03	0.00	0.80	1.20	0.30	0.00	0.00	3.03
892	37.55	0.80	7.54	0.85	9.27	17.70	0.00	7.71	5.60	2.20	1.20	2.24	5.70	30.94
975	2.51	0.60	3.19	68.90	0.19	9.09	0.34	2.55	4.60	0.20	0.30	6.61	0.00	12.28

Table II.1.5 Quantitative XRD results obtained from Rietveld refinement B5

Depth	Anhydrite	Celestine	Chlorite	Dolomite	Gypsum	Illite	Magnesite	Muscovite	Orthoclase	Plagioclase	Pyrite	Quartz	Smectite	Total Clay
115	47.76	0.40	5.27	0.00	1.96	8.61	13.25	5.54	3.30	0.90	0.20	11.15	0.00	13.88
120	34.52	0.40	20.81	0.00	1.03	8.32	11.62	4.80	2.60	0.70	0.30	13.28	0.00	29.13
145	19.14	0.80	22.22	0.33	0.35	26.77	9.76	2.88	3.50	0.40	0.20	4.23	8.52	57.51
155	11.95	0.70	25.81	0.57	0.30	22.92	10.03	3.28	2.50	0.60	0.00	4.91	16.46	65.19
190	18.38	1.10	20.28	0.58	1.85	20.36	10.05	5.44	5.50	0.80	0.20	4.07	10.89	51.53
205	29.60	0.80	4.24	0.69	0.00	26.00	21.19	3.91	6.50	0.30	0.70	4.33	1.50	31.74
255	51.63	0.60	5.10	0.39	0.14	10.56	10.90	4.68	5.30	0.90	1.10	3.02	4.18	19.84
285	26.99	0.70	23.95	0.62	0.73	16.44	8.52	4.73	4.50	0.50	0.40	3.61	8.21	48.60
305	33.79	0.60	25.67	0.00	1.50	8.42	7.59	3.51	3.40	1.00	0.60	6.31	5.94	40.03
355	8.43	0.80	20.70	0.77	0.29	24.12	22.27	4.20	5.80	0.50	0.40	4.63	6.99	51.81
398	14.22	0.60	4.65	0.70	0.57	23.66	37.33	3.42	7.40	1.10	0.40	5.63	0.30	28.61
440	0.50	0.70	28.10	0.37	0.40	18.66	22.11	4.00	5.80	0.40	0.50	5.20	12.52	59.28
445	1.29	0.70	29.05	0.19	1.05	11.10	23.02	5.00	4.50	0.40	0.50	4.37	18.85	59.00
465	68.78	0.30	2.51	0.00	0.78	4.33	11.39	1.01	3.20	1.10	0.60	4.51	0.00	6.84
475	65.75	0.50	2.47	0.31	0.85	4.89	12.82	1.91	3.30	0.40	0.70	4.96	0.00	7.36
485	45.91	0.20	3.14	0.39	1.59	8.87	18.98	3.68	5.30	0.80	0.80	5.31	4.06	16.07

Table II.1.6 Quantitative XRD results obtained from Rietveld refinement B6

Depth	Anhydrite	Celestine	Chlorite	Dolomite	Gypsum	Illite	Magnesite	Muscovite	Orthoclase	Plagioclase	Pyrite	Quartz	Smectite	Total Clay
100	25.03	0.50	21.59	0.89	1.58	14.63	8.51	5.26	2.60	0.50	0.50	11.24	6.94	43.16
110	44.59	0.80	3.28	0.00	0.22	19.40	9.13	2.92	1.70	0.30	0.00	7.31	10.33	33.01
125	7.29	0.80	33.40	0.66	0.12	24.41	7.94	4.61	3.00	0.50	0.00	3.26	14.02	71.83
150	0.55	0.70	43.60	0.69	0.59	13.85	7.50	5.77	2.60	0.20	0.00	1.81	21.87	79.32
205	18.21	0.50	17.92	0.89	2.35	22.20	15.16	4.98	5.50	0.30	0.30	3.67	6.68	46.80
265	24.01	0.70	4.88	0.18	0.00	26.44	18.96	5.51	8.80	0.40	0.70	3.32	5.94	37.26
360	51.96	0.90	5.23	0.34	0.27	11.57	10.29	3.87	4.30	0.70	0.90	3.40	5.00	21.80
365	52.78	0.70	4.99	0.36	0.44	13.99	8.15	4.59	5.30	1.40	0.90	4.25	0.00	18.98
400	3.61	0.70	20.01	0.40	0.52	19.59	6.26	20.70	5.30	2.20	0.40	10.46	9.63	49.23
490	0.46	0.10	39.40	0.27	2.40	11.19	11.60	4.99	3.90	0.30	0.70	4.35	19.29	69.88

II.2   Anhydrite, Gypsum and clay minerals with depth

Figure II.2.1 Distribution of Anhydrite, Gypsum and clay minerals with depth in B2; the un-wrapped OPTV image is shown in the background.
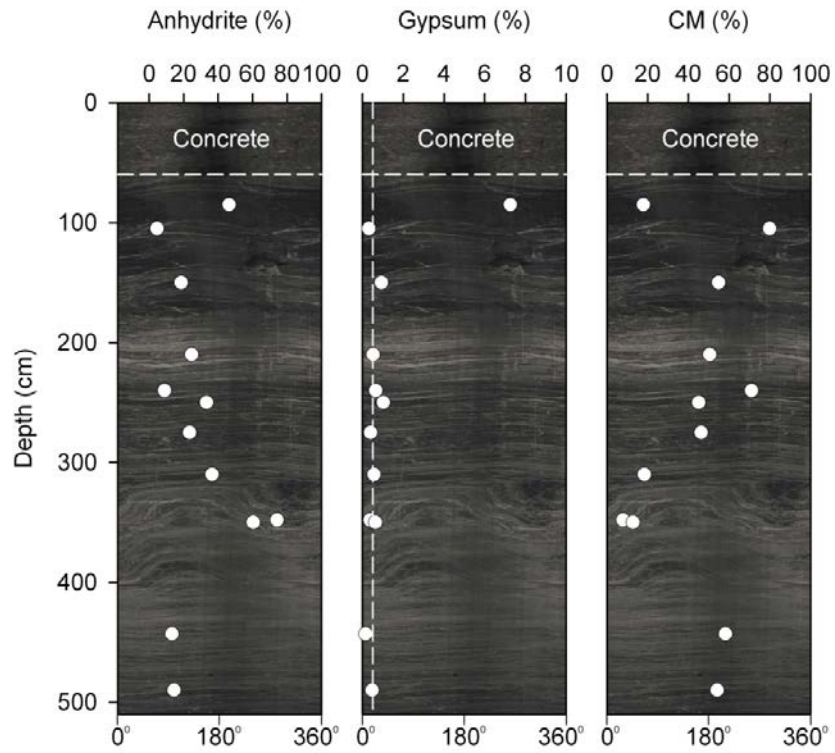

Figure II.2.2 Distribution of Anhydrite, Gypsum and clay minerals with depth in B3; the un-wrapped OPTV image is shown in the background.
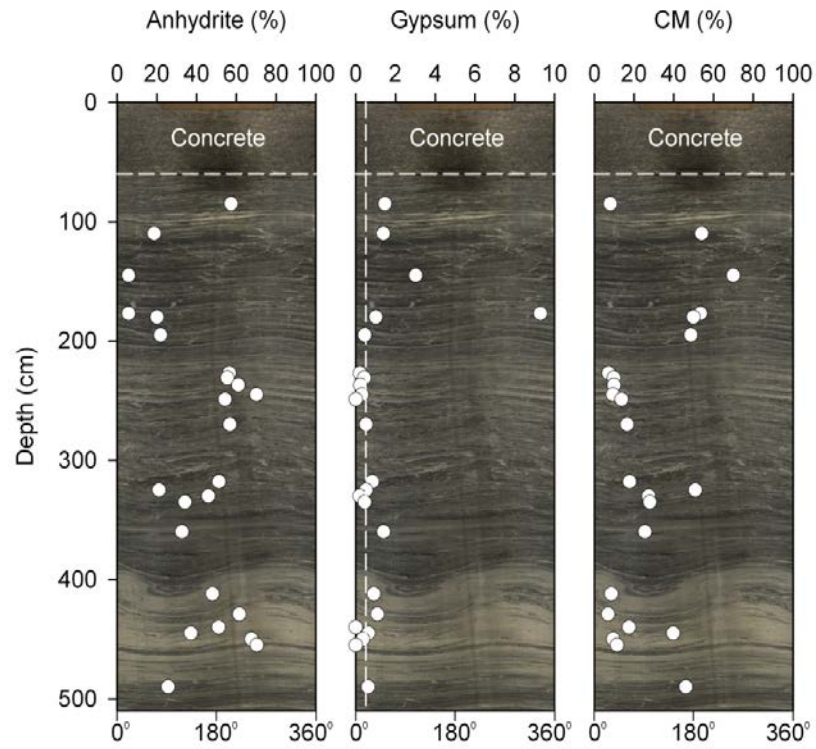
Figure II.2.3 Distribution of Anhydrite, Gypsum and clay minerals with depth in B4; the un-wrapped OPTV image is shown in the background.
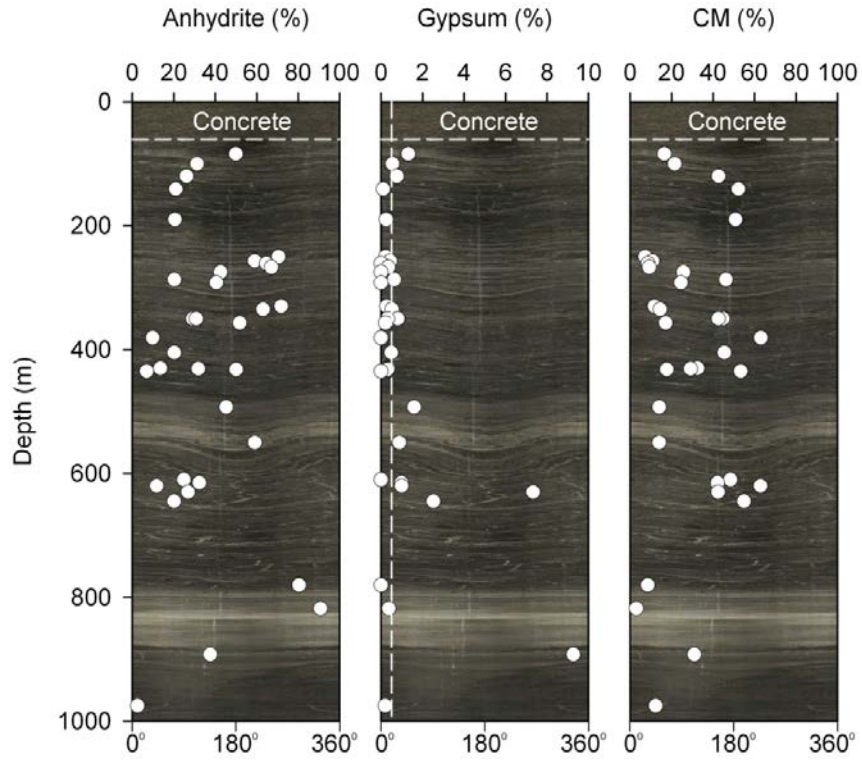

Figure II.2.4 Distribution of Anhydrite, Gypsum and clay minerals with depth in B5; the un-wrapped OPTV image is shown in the background.
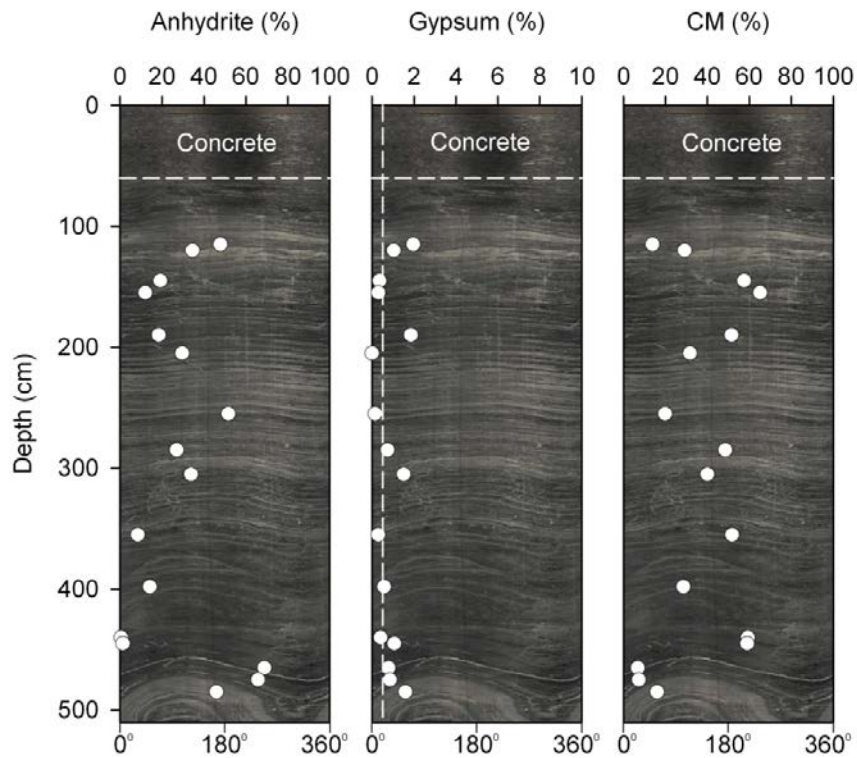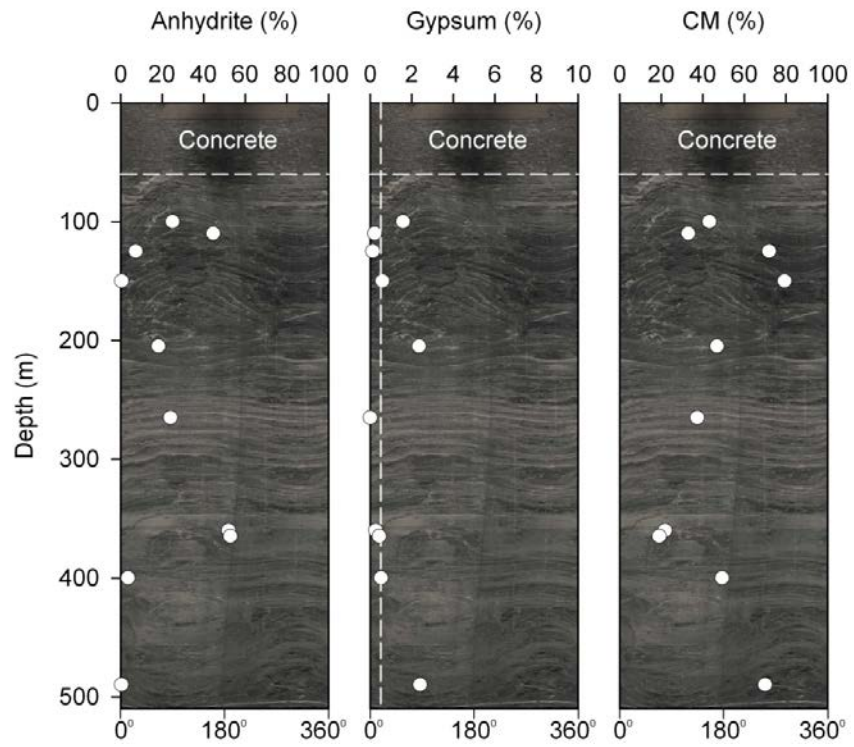
Figure II.2.5 Distribution of Anhydrite, Gypsum and clay minerals with depth in B6; the unwrapped OPTV image is shown in the background.

Abbreviation

Term	Meaning
AE	Acoustic Emission
Ah	Anhydrite
ASTRA	Bundesamt für Strassen
B	Borehole
CEMI	Center of Excellence in Mining Innovation
CL	Clayey matrix
CM	Clay minerals
DATEC	Dipartimento federale dell'ambiente, dei trasporti, dell'energia e delle comunicazioni
DETEC	Département fédéral de l'environnement, des transports, de l'énergie et de la communication
E	Young's Modulus
EMPA	Eidgenössische Materialprüfungs- und Forschungsanstalt
ETH	Eidgenössische Technische Hochschule
Gy	Gypsum
LVDT	Linear variable differential transformer
OPTV	Optical Televiewer
UCS	Unconfined compressive strength
UVEK	Eidgenössisches Departement für Umwelt, Verkehr, Energie und Kommunikation UVEK
VSS	Schweizerischer Verband der Strassen- und Verkehrsfachleute
XRD	X-ray diffraction
Zone A	Zone with macro- and microscopic fibrous gypsum veins
Zone B	Zone with microscopic fibrous gypsum veins
ε_{axial}	Axial strain
ε_{radial}	Radial strain
$\varepsilon_{vol,oil}$	Volumetric strain obtained from oil volume changes
$\sigma_{1, peak}$	Maximum principal stress at specimen failure
σ_3	Minimum principal stress (confining stress)
σ_{CI}	Axial stress at crack initiation
$\sigma_{CI, AE}$	Axial stress at crack initiation obtained from acoustic emission monitoring
$\sigma_{CI, vol}$	Axial stress at crack initiation obtained from volumetric strain response
υ	Poisson's value

Reference List

[1] Anagnostou, G., Pimentel, E., Serafeimidis, K., 2010. Swelling of sulphatic claystones - some fundamental questions and their practical relevance. Geomechanics and Tunnelling 3 (5), 567–572.

[2] Alonso E, I R Berdugo (2006) Degradation and swelling of sulphate-bearing claystones, paper presented at VI CSAMR 2006, Cartanga de Indias, edited by Montero and Colmenares, 211-248.

[3] Vögtli B, P Jordan (1996) Quelldruckentwicklung in Ton- und Sulfatgesteinen, Schweizer Ingenieur und Architekt, 18, 16-180

[4] Grob H (1976) Swelling and heave in swiss tunnels, Bulletin of International Association of Engineering Geologists, 13, 55-60

[5] Steiner W (1993) Swelling rock in tunnels: Characterization, effect of horizontal stresses and construction procedure, I. J. Rock Mech. and Min. Sc. & Geomech Abstr, 30 (4), 361-380

[6] Amstad Ch, Kovari, K (2001) Untertagbau in quellfähigem Fels, Eidgenössisches Department für Umwelt, Verkehr, Energie und Kommunikation (UVEK) & Bundesamt für Strassen (ASTRA), Zürich

[7] Anagnostou G (1995) Seepage flow around tunnels in swelling rock, I. J. Num. Anal. Meth. in Geomech., 19, 705-724

[8] Grob H (1972) Schwelldruck im Belchentunnel, Int. Symp. Für Untertagebau, Luzern, 99-119.

[9] Madsen F T, R Nüesch (1991) The swelling behaviour of clay-sulfate rock, paper presented at 7th Int. Congr. Rock Mech., Aachen, Germany, 285-288.

[10] Madsen, F.T., Flückiger, A., Hauber, L., Jordan, P. and Voegtli, B. 1995. New investigations on swelling rocks in the Belchen tunnel, Switzerland. In: Proceedings of the 8th International Congress on Rock Mechanics, Sept. 25-30, Tokyo, Japan, 263–267.

[11] Alonso E, I R Berdugo (2005) Expansive behaviour of sulphate-bearing clays, paper presented at Intern. Conf. Problematic soils, Famagusta, edited by Bilsel and Nalbantoglu, Eastern Mediterranean University Press, 477-498.

[12] Kaiser P K, Kim B H (2008) Rock Mechanics Challenges in Underground Construction and Mining, paper presented at 1th Sou. Hem. Int. Rock Mech.Sym., Australia, edited by Potvin, Carter, Dyskin and Jeffery, 23-38.

[13] Lockner DA, Moore DE, Reches Z (1992) Microcrack interaction leading to shear fracture, presented at the 33rd U.S. Rock Mechanics Symposium, edited by Tillerson and Wawersik, 908-816, Balkema, Rotterdam, 807-816.

[14] Brace W F, Paulding B R, Scholz C (1966) Dilatancy in fracture of crystalline rocks, J. of Geophys. Res., 71(16), 3939-3953.

[15] Hallbauer D K, Wagner H, Cook N G W (1973) Some Observation Concerning The Microscopic And Mechanical Behaviour Of Quartzite Specimens In Stiff, Triaxial Compression Tests, I. J. of Rock Mech. and Min. Sc. and Geomech. Abst., 10, 713-726.

[16] Scholz C H (1968) Experimental study of the fracturing process in brittle rock, J. of Geophys. Res., 73(4), 1447-1454.

[17] Martin C D, Chandler N A (1994) The progressive fracture of Lac du Bonnet granite, I. J. Rock Mech. and Min. Sc., 31, 643–659.

[18] Fairhurst C, Cook N G W (1966) The phenomenon of rock splitting parallel to the direction of maximum compression in the neighborhood of a surface, Proceedings 1th Congress of the International Society of Rock Mechanics, Lisbon, 687-692.

[19] Bieniawski Z T (1967) Mechanism of brittle failure of rock Part I - Theory of fracture process. I. J. of Rock Mech. and Min. Sc. and Geomech. Abstr., 4(4), 395-406.

[20] Lajtai E Z (1974) Brittle fracture in compression, I. J. of Fracture, 10(4), 525-536.

[21] Tapponier P, Brace WF (1976) Development of stress-induced microcracks in Westerly Granit, I. J. Rock Mech. & Min. Sc., 13, 103-112.

[22] Martin C D (1997) Seventeenth Canadian Geotechnical Colloquium: The effects of cohesion loss and stress path on brittle rock strength, Can. Geotech. J., 34, 698-725

[23] Kaiser P K, Amann F, Steiner W (2010) How highly stressed brittle rock failure impacts tunnel design, paper presented at European Rock Mechanics Symposium 2010, Lausanne, Switzerland, Rock Mechanics and Environmental Engineering, edited by Zhao, Labious, Dudt and Mathier, Taylor and Francis Group, London, ISBN 978-0-415-58654-2, 27-38.

[24] Diederichs M S (2003) Rock fracture and collapse under low confinement conditions, Rock Mech. and Rock Eng., 36 (5), 339-381.

[25] Kaiser P K, Diederichs M S, Martin C D, Sharp J, Steiner W (2000) Underground works in hard rock tunneling and mining, paper presented at GeoEng2000, Melbourne, Australia, 841-926.

[26] Perras M A, Diederichs M S, Amann F (2012) Fracture initiation and propagation in the Quintner Limestone, paper presented at the 46th US Rock Mechanics / Geomechanics Symposium, Chicago, edited by Bobet A, Ewy R, Gadde M, Labuz J, Pyrak-Nolte L, Tutuncu A and Westman E, ARMA 12-401.

[27] Bossart P, Meier P M, Moeri A, Trick T, Mayor J C (2002) Geological and hydraulic characterization of the excavation disturbed zone in the Opalinus Clay of the Mont Terri Rock Laboratory, Engineering Geology 66, 19-38.

[28] Martin C D, Lanyon G W, Bossart P, Blümling P (2004) Excavation Disturbed Zone (EDZ) in Clay Shale: Mont Terri, Mont Terri Technical Report 2001-01.

[29] Blümling P, Bernier F, Lebon P, Martin C D (2007) The excavation damaged zone in clay formations time-dependent behaviour and influence on performance assessment, Physics and Chemistry of the Earth 32, 588-599.

[30] Yong S, Kaiser PK, Loew S (2010) The influence of pre-existing shears on tunnel-induced fracturing, I. J. Rock Mech. and Min. Sc., 47, 894-907

[31] Amann F., E A Button, K F Evans, V S Gischig, M Blümel (2011a) Experimental study of the brittle behavior of clay shale in short-term unconfined compression. Rock Mech Rock Eng, 44 (4), 415-430

[32] Amann F, P K Kaiser, E A Button (2011b) Experimental study of the brittle behavior of clay shale in rapid confined compression. Rock Mech Rock Eng, 44 (1), 21-33

[33] Nussbaum Ch, P Bossart, F Amann, Ch Aubourg (2011) Analysis of tectonic structures and excavation induced fractures in the Opalinus Clay, Mont Terri underground rock laboratory (Switzerland), Swiss Journal of Geosciences, 104 (2), 187-210.

[34] Niandou H, Shao JF, Henry JP, Fourmaintraux D (1997) Laboratory Investigation of the Mechanical Behavior of Tournemire Shale, I. J. Rock Mech. & Min. Sc., 34(1), 3-16.

[35] Valès F, Minh DN, Gharbi H, Rejeb A (2004) Experimental study of the influence of the degree of saturation on physical and mechanical properties in Tournemire shale (France), Applied Clay Science, 26, 197-207.

[36] Schwenk I (2009) Interaktion zwischen Sprödbruchbildung im Gipskeuper und Quellverhalten im Tunnelbau, M.Sc.-Thesis, ETH Zurich, 2009.

[37] Amann F, Kaiser P K, Steiner W (2010) Triggering swelling potential of anhydrite clay rocks by brittle failure processes, paper presented at European Rock Mechanics Symposium 2010, Lausanne, Switzerland, Rock Mechanics and Environmental Engineering, edited by Zhao, Labious, Dudt and Mathier, Taylor and Francis Group, London, ISBN 978-0-415-58654-2, 339-342.

[38] Steiner W, P K Kaiser, G Spaun (2010) Role of brittle fracture on swelling behavior of weak rock tunnels: hypothesis and qualitative evidence, Geomechanics and Tunnelling, 3(5), 583-596.

[39] Steiner W, P K Kaiser, G Spaun (2011) Role of brittle fracture on swelling behavior of weak rock tunnels: evidence from tunnelling case histories, Geomechanics and Tunnelling, 4(2), 141-156.

[40] I.S.R.M. (1979) Suggested Methods for Determining the uniaxial compressive strength and deformability of rock materials, I. J. of Rock Mech. and Min. Sc. and Geomech. Abst., 16(2), 135-140.

[41] Eberhardt E, Stead D, Stimpson B, Read R S (1998) Identifying crack initiation and propagation thresholds in brittle rock, Can. Geotech. J., 35, 222-233.

[42] Nicksiar M, C D Martin (2012) Evaluation of methods for determining crack initiation in compression tests on low-porosity rocks, Rock Mech. Rock Eng., , 607-617.

[43] Klinkenberg M, Kaufhold S, Dohrmann R, Siegesmund S (2009) Influence of carbonate micofabric on the failure strength of claystones, Engineering Geology, 107, 42-54.

[44] Mogi K (1962) Study of elastic shocks caused by the fracture of heterogeneous materials and its relations to earthquake phenomena, Bulletin of the Earthquake Research Institute, 40, 125-173.

[45] Jordan, P. and Nüesch, R. (1989) Deformation structures in the Muschelkalk Anhydrites of the Schafisheim Well (Jura Overthrust, Northern Switzerland). Eclog. geol. Helv. 82,429-454.

[46] Nüesch, R, Steiner. W. and Madsen, F.T. 1995. Long time swelling of anhydritic rocks: mineralogical and microstructural evaluation. In: Proceedings of the 8th International Congress on Rock Mechanics, Sept. 25-30, Tokyo, Japan. p. 133-138.

[47] Scheiber, J. Stosch, H. Schwotzer, M. Eckhardt, J. Kölbel, T. Burkhardt, H. (2011) Detektion von Anhydrit in Bohrklein – Vergleich verschiedener Analysekonzepte". In: BBR Sonderheft Oberflächennahe Geothermie, 18-27.

Projektabschluss

Schweizerische Eidgenossenschaft
Confédération suisse
Confederazione Svizzera
Confederaziun svizra

Eidgenössisches Departement für
Umwelt, Verkehr, Energie und Kommunikation UVEK
Bundesamt für Strassen ASTRA

FORSCHUNG IM STRASSENWESEN DES UVEK
Formular Nr. 3: Projektabschluss

erstellt / geändert am: 29.05.2013

Grunddaten

Projekt-Nr.:   ASTRA 2011/006

Projekttitel: Fractures and in-situ fracture observations in Gipskeuper

Enddatum: 15.05.2013

Texte

Zusammenfassung der Projektresultate:

Die felsmechanische Analyse in dieser Studie hat gezeigt, dass bei relativ geringen Differentialspannungen das Bruchverhalten von der Festigkeit der tonigen Matrix bestimmt wird, in der erste Mikrorisse entstehen. An Prüfkörper mit einem heterogenen Gefüge aus diskreten Tonsteinlagen und Anhydrit-Venen wurde beobachtet, dass die Differentialspannung zur Initialisierung von Mikrorissen vom Tongehalt abhängt. Bei einem Tongehalt > 7-10% entstehen erste Mikrorisse bei einer relativ konstanten Differentialspannung im Bereich zwischen 4 und 13 MPa. Variationen in der Grenzspannung zur Rissinitialisierung stehen sehr wahrscheinlich im Zusammenhang mit der Mikrostruktur und dem Anhydrit-Gehalt der tonigen Matrix sowie Spannungs- und Dehnungs-Heterogenitäten als Folge zunehmender kompressiver Spannungen. Für einen Tongehalt < 7-10% nehmen sowohl die Grenzspannungen zur Rissinitialisierung als auch die Spitzenfestigkeiten deutlich zu. Dünnschliffanalysen von Prüfkörpern nach mechanischer Belastung deuten darauf hin, dass bei kompressiven Belastungen oberhalb der Grenzspannung zur Rissbildung die Felsstruktur einen markanten Einfluss auf das Risswachstum, die Risszusammenschliessung und die Spitzenfestigkeiten hat. In Abhängigkeit der Anhydrit-Venendichte, der Venenverteilung und Venenorientierung kann das Risswachstum an Anhydrit-Venen stoppen, wodurch Risse entlang von Venen entstehen können, oder Risse die Venen durchschlagen. Diese Risse führen häufig zur Vernetzung von mikro-geschädigten Regionen im Prüfkörper. Da Venen grössere Festigkeiten als die tonige Matrix aufweisen nimmt mit zunehmender Venendichte die Spitzenfestigkeit zu, obgleich erste Mikrorisse bereits bei niedrigen Differentialspannungen entstehen.
Die Analyse der Bohrkerne und der optischen Bohrlochscanner-Aufnahmen haben gezeigt, dass offene, makroskopische oder mikroskopische Risse kaum zu finden sind. Im Tiefenbereich zwischen der Tunnelsohle und maximal 2.35 m wurden Risse angetroffen, welche mit Fasergips verheilt waren. Derartige Risse sind ausschliesslich in der tonigen Matrix zu finden und konnten keinem prä-existierenden Risssystem zugeordnet werden. Nur wenige tektonische Strukturen wie zum Beispiel Bruch- oder Schichtflächen waren mit Fasergips verfüllt. Diese Erkenntnisse weisen darauf hin, dass die in den ersten Dezimetern der sechs Bohrungen untersuchten Risse neu entstanden sind.
Der Grossteil der neu entstandenen Mikro-Risse in den oberen Bohrlochdezimetern zeigten zudem Reaktionsränder von etwa 0.05-0.1 mm Mächtigkeit. Fasergips wurde nahezu ausschliesslich in solchen Rissen gefunden. Die chemische Umwandlung der tonigen Matrix wird im Zusammenhang mit Wasserzirkulation gesehen. Diese Erkenntnisse lassen den Schluss zu, dass die beobachteten Mikrorisse vernetzt sind und präferentielle Fliesswege für die Wasserzirkulation und die Gipsausfällung darstellen.

Schweizerische Eidgenossenschaft
Confédération suisse
Confederazione Svizzera
Confederaziun svizra

Eidgenössisches Departement für
Umwelt, Verkehr, Energie und Kommunikation UVEK
Bundesamt für Strassen ASTRA

Zielerreichung:

Die Ziele der Studie lagen darin Bruchprozesse im Gipskeuper, insbesondere die Rissinitialisierung experimentell zu untersuchen sowie in-situ beobachtete mikroskopische und makroskopische Risse im Bezug auf ihre Entstehung und ihren Einfluss auf die Wassewegigkeit zu charakterisieren. Der Grossteil der Schlüsselfragen zu dieser Studie konnte mit den Methoden und im Rahmen des geplanten Budget zufriedenstellen beantwortet werden.

Folgerungen und Empfehlungen:

Weiterführend zu dieser Studie ist zu empfehlen, dass die Rissbildung während des Baus eines Tunnels im Gipskeuper und deren Auswirkung auf die Permeabilität mit Abstand zum Tunnel untersucht werden.

Publikationen:

Es sind zwei Publikationen in Internationalen Journalen sowie zwei Konferenzbeiträge geplant. Die Titel dieser Publikationen stehen derzeit noch nicht fest.

Der Projektleiter/die Projektleiterin:

Name: Amann   Vorname: Florian

Amt, Firma, Institut: ETH Zürich, Engineering Geology

Unterschrift des Projektleiters/der Projektleiterin:

Forschung im Strassenwesen des UVEK: Formular 3   Seite 2 / 3

Schweizerische Eidgenossenschaft
Confédération suisse
Confederazione Svizzera
Confederaziun svizra

Eidgenössisches Departement für
Umwelt, Verkehr, Energie und Kommunikation UVEK
Bundesamt für Strassen ASTRA

FORSCHUNG IM STRASSENWESEN DES UVEK

Formular Nr. 3: Projektabschluss

Beurteilung der Begleitkommission:

Beurteilung:

Die Zielsetzungen des Forschungsprojekts wurden erfüllt. Der Bericht bietet vertiefte Einblicke in die Prozesse Rissbildung und Gipskristallwachstum im Gipskeuper. Das Forschungsprojekt liefert wichtige Erkenntnisse auf Niveau Grundlagenforschung betreffend den Auslösemechanismen von Quellhebungen und Zwängungen bei Tunnelbauten im Gipskeuper.

Umsetzung:

In-situ Kernaufnahmen, Bohrlochscanner, XRD-Analysen, Dünnschliffanalysen, Einaxial- und Triaxialversuche, akustische Bruchaufzeichnung

weitergehender Forschungsbedarf:

Detailliertere Aufklärung der Mechanismen der Kristallisation von Gips im Kontext des Tunnelbaus in sulfatreichen Tongesteinen mit Fokus Transportprozesse und Hydrochemie. Welche Bedingungen (Spannungszustände) und welche Strömungsverhältnisse und Konzentrationen sind nötig. Ausweitung der Versuche auf Paramente und Tunnelfirste.
Erarbeitung Grundlagen Dimensionierung für zukünftige Bau- und Sanierungsprojekte im Gipskeuper: Empfehlungen zur Querschnittsgestaltung inkl. Ausbauwiderstände sowie zur Vortriebswahl und zulässiger Gebirgsentlastung. Empfehlung betreffend Vorauserkundungsmassnahmen.

Einfluss auf Normenwerk:

Zurzeit ist die Umsetzung in einer Norm nicht vorgesehen.

Der Präsident/die Präsidentin der Begleitkommission:

Name: Folly   Vorname: Matthias

Amt, Firma, Institut: Bundesamt für Strassen ASTRA

Unterschrift des Präsidenten/der Präsidentin der Begleitkommission:

Verzeichnis der Berichte der Forschung im Strassenwesen seit 2009

Bericht-Nr.	Projekt Nr.	Titel	Datum
1356	SVI 2007/014	Kooperation an Bahnhöfen und Haltestellen *Coopération dans les gares et arrêts* *Coopération at railway stations and stops*	2011
1362	SVI 2004/012	Aktivitätenorientierte Analyse des Neu-verkehrs Activity oriented analysis of in-duced travel demand Analyse orientée aux acitivtés du trafic induit	2012
1361	SVI 2004/043	Innovative Ansätze der Parkraukmbewirtschaftung Approches innovantes de la gestion du stationnement Innovative approaches to parking management	2012
1357	SVI 2007/007	Unaufmerksamkeit und Ablenkung: Was macht der Mensch am Steuer? Driver Inattention and Distraction as Cause of Accident: How do Drivers Be-have in Cars? L'inattention et la distraction: comment se comportent les gens au volant?	2012
1360	VSS 2010/203	Akustische Führung im Strassentunnel Acoustical guidance in road tunnels Guidage acoustique dans les tunnels rou-tiers	2012
1365	SVI 2004/014	Neue Erkenntnisse zum Mobilitätsverhalten dank Data Mining? De nouvelles découvertes sur le compor-tement de mobilité par Data Mining? New findings on the mobility behavior through Data Mining?	2011
1359	SVI 2004/003	Wissens- und technologientransfer im Verkehrsbereich Know-how and technology transfer in the transport sector Transfert de savoir et de technologies dans le domaine des transports	2012
1363	VSS 2007/905	Verkehrsprognosen mit Online -Daten Pronostics de trafic avec des données en temps réel Traffic forecast with real-time data	2011
1367	VSS 2005/801	Grundlagen betreffend Projektierung, Bau und Nachhaltigkeit von Anschlussgleisen Principes de bases concernant la concep-tion, la construction et la durabilité de voies de raccordement Basic Principles on the Design, Construc-tion and Sustainability of Sidings	2011
1370	VSS 2008/404	Dauerhaftigkeit von Betongranulat aus Betongranulat	2011

1373	VSS 2008/204	Vereinheitlichung der Tunnelbeleuchtung	2012
1369	VSS 2003/204	Rétention et traitement des eaux de chaussée	2012
648	AGB 2005/023 + AGB 2006/003	Validierung der AAR-Prüfungen für Neubau und Instandsetzung	2011
1371	ASTRA 2008/017	Potenzial von Fahrgemeinschaften *Potentiel du covoiturage* *Potential of Car Pooling*	2011
1374	FGU 2004/003	Entwicklung eines zerstörungsfreien Prüfverfahrens für Schwiessnähte von KDB *Dévelopment d'une méthode d'éssais non-déstructif pour des soudures de membranes polymères d'étanchéité* *Development of a nondestructive test method for welded seams of polymeric sealing membranes*	2012
1375	VSS 2008/304	Dynamische Signalisierungen auf Hauptverkehrsstrassen *Signalisations dynamiques sur des routes principales* *Dynamic signalling at primary distributors*	2012
1376	ASTRA 2011/008_004	Erfahrungen im Schweizer Betonbrückenbau *Expériences dans la construction de ponts en Suisse* *Experiences in Swiss Bridge Construction*	2012
1379	VSS 2010/206_OBF	Harmonisierung der Abläufe und Benutzeroberflächen bei Tunnel-Prozessleitsystemen *Harmonisation of procedures and user interface in Tunnel-Process Control Systems* *Harmonisation des processus et des interfaces utilisateurs dans les systèmes de supervision de tunnels*	2012
1380	ASTRA 2007/009	Wirkungsweise und Potential von kombinierter Mobilität *Mode of action and potential of combined mobility* *Mode d'action et le potentiel de la mobilité combinée*	2012
1381	SVI 2004/055	Nutzen von Reisezeiteinsparungen im Personenverkehr *Bénéfices liés à une réduction des temps de parcours du trafic voyageur* *Benefits of travel time savings in passenger traffic*	2012

1383	FGU 2008/005	Einfluss der Grundwasserströmung auf das Quellverhalten des Gipskeupers im Chienbergtunnel *Influence de l'écoulement souterrain sur le gonflement du Keuper gypseux dans le Tunnel du Chienberg* *Influence of groundwater flow on the swelling of the Gipskeuper formation in the Chienberg tunnel*	2012
1386	VSS 2006/204	Schallreflexionen an Kunstbauten im Strassenbereich *Réflexions du trafic routier aux ouvrages d'art* *Noise reflections on structures in the street*	2012
1387	VSS 2010/205_OBF	Ablage der Prozessdaten bei Tunnel-Prozessleitsystemen *Data storage in tunnel process control systems* *Enregistrement ds données de systèmes de supervision de tunnels*	2012
649	AGB 2008/012	Anforderungen an den Karbonati-sierungswiderstand von Betonen *Exigences par rapport à la résistance à la carbonatationdes bétons* *Requirements for the carbonation resistance of concrete mixes*	2012
650	AGB 2005/010	Korrosionsbeständigkeit von nichtrosten-den Betonstählen *Résistance à la corrosion des aciers d'armature inoxydables* *Use of stainless steels in concrete structures*	2012